1

Nanometer Scale

The methodologies implemented for the elaboration and analysis of materials or objects on the nanometer scale are part of nanotechnologies. The fundamental research conducted at this scale, which is referred to as nanoscience, generates knowledge on the innovative properties associated with nanometer dimensions, as well as on the relevant methods of analysis. Nanotechnologies concern technologies used for the industrial manufacturing of devices carrying a commercial and societal value, while following the safety limits applicable to nano-objects manipulation and use. It is essentially multidisciplinary and relies on chemistry, physics, materials science, simulation, information and communication technologies, engineering science and many other disciplines. Mechatronics and robotics for terrestrial and spatial transportations and the technologies for connected objects are concerned by the developments in nanotechnologies. Working at the nanometer scale requires especially adapted metrology, as measurements of the properties of nanodevices often lead to relative values whose standard deviation is of the same order of magnitude as the measured value. Indeed, in most cases, to qualify the measured values, simulations should be conducted in parallel with the measuring process.

1.1. Introduction

Historically, the landmark of the foundation of nanotechnology is the lecture given by R. Feynman, recipient of Nobel Prize for Physics in 1965 for his contribution to quantum electrodynamics. The lecture was entitled "There is plenty of room at the bottom", and was given on December 29, 1959, at the annual meeting of the American Physical Society at California

Institute of Technology. On this occasion, he stated: "The principles of physics, as far as I can see, are not against the possibility of manipulating things atom by atom".

The term "nanotechnology" was coined by N. Taniguchi in 1974 [TAN 74], to describe the processes of thin-film deposition during the elaboration of "wafers" of semiconductors. The scanning electron microscope developed in 1981 [BIN 82a, BIN 82b, BIN 83 BIN 86a], for whose invention G. Binnig and H. Roher received the Nobel Prize for Physics in 1986, can be used to visualize surfaces at atomic or nanometer scale. In retrospect, some sort of Gant chart can be drawn to quantify the time lapse of over two decades between Feynman's idea in 1959 on atom manipulation, the elaboration in the 1970s of materials or nano-objects structured at nanometer scale, including the invention of the term nanotechnology in 1974 and, finally, the development of the instrument enabling the effective visualization and manipulation of the atom, in 1981. Two major fields of investigation corresponding to different temporalities can be identified: a first phase for the controlled synthesis or elaboration of nano-objects, and a second phase for measurement and analysis. The acquisition of knowledge used by the engineer to implement innovations requires the development of imaging tools and especially of nanometer-scale analysis methods. The efficiency of the overall scientific effort depends on the availability of multidisciplinary competences, which involves a systemic approach.

Some of the most fascinating problems in all science fields involve multiple temporal or spatial scales (cosmology, materials science, elementary particles, etc.) so that in the science field, the scales of interest for scientists range from Planck length of 10^{-35} m to the distance of 10^{24} m, which, in cosmology, corresponds to the diameter of the volume of observation (local group) of the Universe since the Big Bang.

In the field of technologies and engineering sciences, the invention of the transistor in the 1950s by J. Bardeen and W. Brattain [BAR 48] and W. Shockley [SHO 49] of Bell Laboratories opened the way to micro-technologies. The integration density of transistors consequently doubled every two years, in accordance with Moore's law [MOO 65]. As shown in Figure 1.1, the following stage of technology development is in the field of nanotechnologies, a source of innovations for the 21st-Century industry.

Figure 1.1 gives an overview of the various scales (on the X axis) that should be considered in materials sciences and in scientific subjects (quantum physics, chemistry, materials sciences and engineering) that elaborate the knowledge in the considered field (nanoscopic, microscopic, mesoscopic, macroscopic). The scale of interest for technological applications is naturally the macroscopic scale, the dimension perceived at human scale in society. The relations between material structure and properties determine the behavior of the material at the macroscopic scale. Figure 1.1 also indicates the properties or phenomena studied at various scales by simulation, providing a non-exhaustive list of several theoretical models developed for apprehending the behavior of the material (*ab initio* calculations, molecular dynamics, Monte Carlo simulation, dislocation dynamics and Monte Carlo dynamics, polycrystalline models, finite element method).

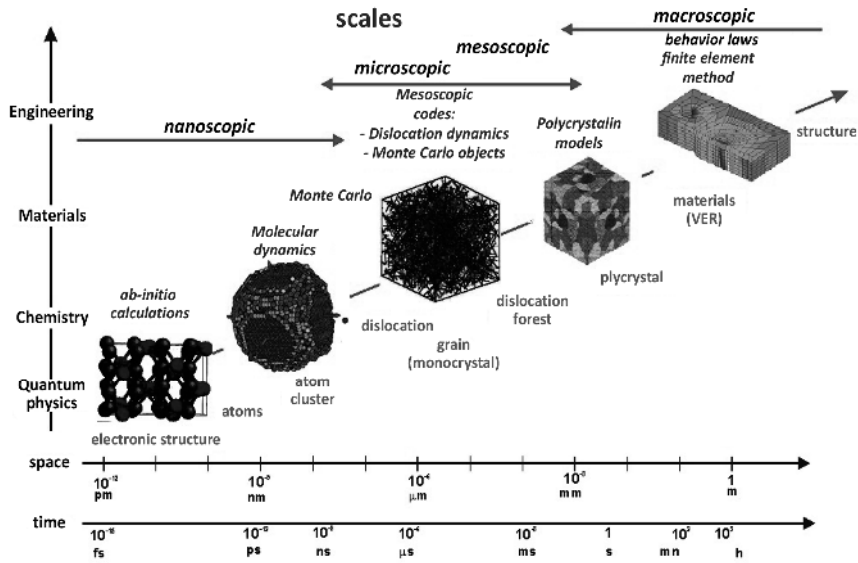

Figure 1.1. *Various spatial and temporal scales in materials sciences. For a color version of this figure, see www.iste.co.uk/dahoo/metrology1.zip*

The term nano originates in the Greek term "nannos" or "νανvoζ", which means "excessively short or dwarf". In metrology, which is the science of measurement, a nanometer corresponds to 10^{-9} m. While human hair size of 10^{-4} m is small on the meter scale, it is huge at the nanometer

scale. It is the scale corresponding to molecules. It was agreed to classify any object whose size ranges between 10^{-10} m and 10^{-7} m as belonging to the nanometer scale, though the term nano more generally describes measured dimensions that range between 1 nm and 100 nm. This interval contains, for example, dimensions corresponding to the size of viruses (100 nm), deoxyribonucleic acid or DNA (10 nm) and molecular structures (1 nm). The term nano generated a large number of terms whose prefix is nano. The terms employed in this book are mainly nanoscale, nanometric, nanosciences and nanotechnologies, thus referring the reader to works specifically dedicated to nanosciences and nanotechnologies.

Nanoresearch is conducted in many domains: nanoelectronics, modeling, simulation and design of nano-objects, nanobiotechnologies, nanomedicine, nanophotonics, nano-characterization, nanometrology, nanolithography, nano-fabrication of nano-objects, nanotoxicology in health, environment and nano-security fields. The knowledge and know-how related to all these domains can be found in numerous works that were published after the emergence of nanoscience in the 2000s. The readers who are interested in gaining in-depth knowledge in a specific field are referred to [RAT 02, LAH 04, DUP 06, LAH 06, LAH 07, LAH 10, LOU 16, KNE 20, LEE 20]. Being in continuous and rapid evolution in all the disciplines since 2000, nanoscience and nanotechnologies are the object of many calls for projects throughout the world.

On the nanometer scale, the classical theories of Newtonian mechanics are not adapted and the principles of quantum mechanics should be applied for the interpretation of the mechanics of physics and chemical phenomena. In classical mechanics, distant interactions are modeled by forces that act instantaneously throughout the space. While possible according to classical theory, simultaneous measurement of position and speed is not possible in quantum mechanics, following Heisenberg's uncertainty principle $\Delta x \Delta p \approx h/2\pi$, which must hold.

On the other hand, Maxwell's theory of the electromagnetic field, which is built in terms of electric and magnetic fields, is in agreement with the quantum description for matter–light interaction, as shown in [DAH 16].

In his works on the attraction of spheroids, Laplace shows that "the calculation with partial differences" can be used to locally formulate the interaction between two masses in terms of potentials. Laplace writes on

page 358 [LAP 94] that "a sphere attracts an external point as if all its mass were united in its center" and on page 382 [LAP 94] that "In the planetary theory, the objective is not to determine their equilibrium in absolute space, but only the equilibrium of all their parts around their centers of gravity". Nevertheless, if gravitation is formulated in terms of fields or potential, as Laplace did in 1785 [LAP 94] to locally describe gravitational force, classical mechanics may be regarded as an approximation of the general theory of relativity. Unlike Maxwell formalism, which describes the electromagnetic phenomena in terms of electric and magnetic fields, it cannot be directly inserted in the quantum theory.

The transition from classical mechanics to QM is possible through the principle of correspondence between Poisson brackets defined in Hamiltonian mechanics and the commutators between operators acting in Hilbert space according to Heisenberg formalism. The formulation of the theory of gravitation in terms of gravitational fields as used in general relativity should be compared to the quantum field theory, which is more appropriate for the description of interactions between elementary particles.

All these considerations show that different formalisms were developed in order to describe the physical phenomena on various scales. To innovate in the field of nanotechnologies, the engineer should therefore apprehend and master the physical concepts that are currently being developed in research laboratories.

On the nanometer scale, implementing a technique for the measurement of a physical property is not a simple task, and when a measurement is made, its repeatability is not guaranteed. In general, in the absence of a standard as a reference, accuracy is hardly reached. And if precision is achievable, it requires a lot of time to be set up at the nanometer scale. Consequently, there are few measurements really achieved and the implementation of measurement instruments is not an easy task. Furthermore, measurements should also rely on theoretical models.

Experimental and theoretical examples for the study of materials at the nanometer scale are given in Chapter 6 of [DAH 16]. The first chapter of [DAH 16] provides an overview of the elaboration, characterization and analysis techniques relevant to nanotechnologies. There are two major fields of investigation in nanotechnologies, namely the synthesis or elaboration of nano-objects while controlling the manufacturing process and the process of

characterization and analysis, which involves the development of imaging and analysis tools at the nanometer scale. These studies rely on quantum mechanics principles.

Based on research works conducted in the laboratories of the University of Versailles as part of fundamental research [DAH 04a, DAH 04, FRA 05, HAM 06, HAM 07, NOU 07] or in relation with the industrial environment, three examples are considered to illustrate three techniques for the elaboration of nanomaterials samples: spin coating, cathode sputtering and laser ablation. Similarly, four techniques for sample study and characterization are presented: transmission electron microscope (TEM), scanning electron microscope (SEM), atomic force microscope (AFM) and ATR spectroscopy.

1.2. Sample elaboration

The samples studied in nanosciences are manufactured either in bulk form or as a thin film deposited on a substrate by chemical, physical and chemical or physic-chemical processes. A sample is classified as a nanomaterial if at least one of its dimensions ranges between 1 and 100 nm.

A thin film always involves a substrate, irrespective of the procedure employed for its manufacture (it may happen that a thin film is separated from its substrate). Consequently, the substrate has a very strong influence on the structural properties of the deposited film. The nature of the substrate influences the physical properties of a mono-material thin film, all other characteristics being the same. Thus, the physical properties of a thin film are slightly different depending on whether it is deposited on an amorphous insulating substrate, such as glass, or on a silicon monocrystalline substrate, for example. It is worth noting that a thin film is anisotropic by construction.

There are numerous methods for preparing thin films. Only those most commonly used in the field of electronics and technology in relation to transport, optics, magneto-optics and heat properties are mentioned here. The main manufacturing methodologies used by the manufacturers of active or passive electronic components are based on physical processes for the deposition of material on a substrate. Therefore, the thin film increases in thickness from zero and this growth must be controlled.

In the case of chemical deposition, the films grow through a chemical reaction between a substrate maintained at an optimal deposition temperature in the presence of an inert gas in a low pressure preparation chamber and a precursor fluid, which results in a solid film that covers the whole surface. Depending on the precursor phase, chemical deposition is differently classified. Some examples of coating are spin coating, dip coating, atomic layer deposition (ALD), electro-deposition and, finally, chemical vapor deposition (CVD), and the variants associated with CVD differ depending on the process used to initiate the chemical reactions and on the process conditions, such as plasma-enhanced (PECVD), metallo-organic (MOCVD) and very low-pressure CVD.

In the physical deposition processes, the material to be deposited is generated in solid, liquid or gaseous state, and then it is physically carried on the surface of the substrate. This stage takes place in a preparation chamber under vacuum. The processes through which the matter to be deposited is generated are essentially mechanical, thermal or electromechanical, such as thermal evaporation, sputtering or ion plating. The choice of the deposition process depends on a certain number of factors, such as the substrate structure, the deposition temperature, the deposition rate and the source of material. The deposited films can be structured by other techniques, such as photolithography.

Two large families of physical methods can be distinguished in practice. One of them involves a carrier gas that moves the material to be deposited from a recipient to the substrate and is related to scattering techniques used in the manufacture of active components. The other one involves a very low-pressure environment and the material to be deposited is carried by an initial thermal or mechanical pulse. To elaborate a thin film, we must choose the material to be deposited, the substrate and the deposition technique.

The three most common thin-film deposition techniques are cathode sputtering, molecular beam epitaxy and laser ablation.

– *Cathode sputtering*. A target is bombarded with an inert gas (argon) in order to sputter the atoms in the target. Applying a potential difference between the target (cathode) and the substrate (anode), the sputtered atoms are accelerated and deposited on the substrate.

– *Molecular beam epitaxy*. Conducted under high vacuum, this method involves the evaporation of the material to be deposited by heating, radiation or electron bombardment.

– *LASER ablation*. Groups of atoms in the target are "evaporated" by means of a high-fluence LASER beam.

Unlike magnetron or diode sputtering, which relies on a mechanical principle of atomic or more precisely ion bombardment, vacuum or ultra-high vacuum evaporation relies on a thermal principle. Heat brings matter to its melting point and then to its evaporation point.

Vacuum evaporation relies on two elementary processes, namely the evaporation of a heated source followed by condensation to solid state of the matter evaporated on the substrate. Matter heating can be generated by several techniques leading to its evaporation: Joule effect, through which a current of normally several hundred Amperes passes through the matter to evaporate, electron bombardment (evaporation using an electron gun), effusion evaporation, magnetron cathode sputtering, diode cathode sputtering and laser ablation evaporation.

Molecular beam epitaxy (MBE) is conducted under ultra-high vacuum. It involves the evaporation of the material to be deposited by heating, radiation or electron bombardment on a substrate. With this technique, one or several molecular beams of atoms can be directed towards the substrate to achieve epitaxial growth. It enables the growth of nano-structured samples of several cm^2 at a speed of about one atomic monolayer per second. An MBE setup consists of an introduction airlock equipped with a turbomolecular pump and a preparation chamber containing:

– a gun enabling ion bombardment of the surfaces (Ar+ ions of energy ranging between 1 and 8 keV);

– a furnace enabling heating up to 1,800°C by combining Joule effect up to 500°C and electron bombardment for temperatures beyond;

– a micro-leakage valve to introduce gas in the chamber. The temperature during growth is measured by a thermocouple and/or an infrared thermometer.

To illustrate the thin-film deposition techniques at nanometer scale, descriptions of spin coating, cathode sputtering and laser ablation techniques are detailed below.

1.2.1. *Physical and chemical method: spin coating*

One method for chemically preparing a polymer sample in the form of thin film on a substrate at nanoscale is spin coating. It is worth noting that there are several methods for preparing thin films, depending on the nature of the polymer, thickness and application, namely spin coating, dip coating or serigraphy.

This section presents the process used in a thesis work at the University of Versailles St Quentin, in a joint project with the transportation industry, funded within MOVEO, a competitiveness cluster [KHE 14]. The embedded electronics systems from car suppliers in the automotive industry comprise plastic materials, notably for coating electronic components. To ensure the reliability of the encapsulated devices, the quality of the plastic cases of the electronic components must be controlled. Due to their low costs and high performances, electronic cases are essentially made of plastic materials. In this respect, plastic cases are most often made from epoxy resin and silica. Water absorption is the first cause of deterioration of electronic cases, resulting in the formation of cracks and delaminations of the coating. Aging studies in humid or aqueous environments contribute to a better understanding of the various paths corresponding to physical or chemical degradations of resins. The presence of water more or less related to the polymer is identified as a main cause.

The study of interfaces at the nanometer scale was conducted on silicone gels used for the encapsulation of electronic circuits. These polysiloxane-based gels are polymers characterized by a silicon–carbon Si–C bond and by a silicon–oxygen Si–O bond. They are very stable at high temperatures ≥180°C and provide an electric insulation of 20 kV/mm, being both resistant to chemical products and moisture proof. The silica surface is characterized by the groups: silanols (Si–OH) and siloxanes (Si–O–Si). Interactions between the reactive functions of the polymer and the silanols of the silica surface are susceptible to appear at the silica surface. On the other hand, the presence of hydroxyl functions on the polymer chain supports the absorption and the fixation of the polymer by hydrogen bond to the surface of the silica particle. A coupling agent is added to modify the silica surface in order to favor the bonds between the organic polymer and the charges. It generally takes the form of an alkoxysilane. During the cross-linkage reaction, this agent forms stable chemical bonds between the polymer and the charges. One of the coupling agents that is currently used in the industry is

glycidyloxypropyltrimethoxysilane (GOTMS). The coupling agent can also be very useful at the interface between metal and resin, as it forms a hydrophobic film at the surface of the metal and enables a very good adhesion between the metal and the resin. The studied polymers were either single-component silicone gels or two-component silicone gels. The characterization of samples by ellipsometry at nanometer scale was presented in Chapter 8 of [DAH 16].

Spin coating is widely used for the deposition of polymer films on electronic components. It involves the deposition by a syringe of a given volume of polymer solution on the surface of a substrate. A vacuum pump enables the fixation by aspiration of the substrate on a rotary support during the rotation for the efficient spread of the film and a mechanical stability of the whole even at 10,000 rpm. The device spinner can reach a rotational speed of 10,000 rpm and an acceleration/deceleration from 1 to 7,500 rpm. The various stages are schematically represented in Figure 1.2.

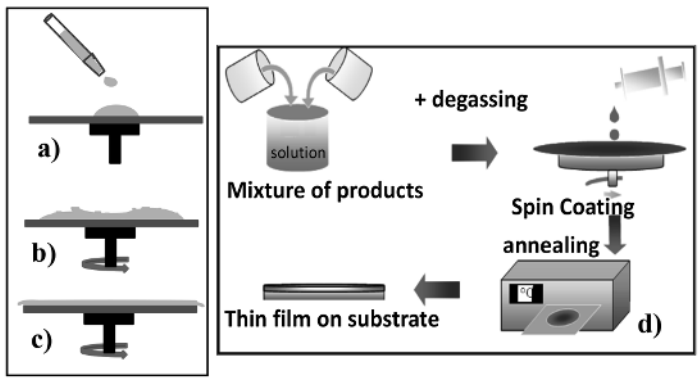

Figure 1.2. *The stages of spin coating technique: a) deposition of volume, b) spreading by rotary spinner, c) homogeneous thin film, d) spin-coating-based manufacturing process. For a color version of this figure, see www.iste.co.uk/dahoo/metrology1.zip*

By spin coating technology, roughness and thickness can be kept under control, their values ranging from about 100 nanometers to several micrometers. Among other factors, the final thickness depends on the concentration of the polymer solution (viscosity) and on the rotational speed

(centrifugal force) of the device. The thickness *d* of a thin film deposited by spin coating is indirectly proportional to the angular speed ω of the spinning plate. It can be written that $d \approx \omega^{-n}$, where the exponent n depends on the solvent. In the absence of evaporation, d varies with time t and speed, such that $d \approx \omega^{-1}t^{-1/2}$ and if the evaporation rate is constant, $d \approx \omega^{-2/3}$. However, it is observed that $d \approx \omega^{-1/2}$. A calibration of the device is required to determine the volume of solution as a function of the desired thickness given the viscosity of the product.

An accurate protocol must be followed before depositing the solutions on the chosen substrate. Quartz (SiO_2) is generally used as a model substrate before trying other substrates that can otherwise be made from ceramics, metal (Al), semiconductor (Si, Ge) or alloy (Cu/Ni, Cu/Ag). Substrates must first be cleaned. If they are not prone to oxidation, an ultrasonic bath is used: the substrate is immersed in water, respecting the allowed volumes between a minimal and a maximal quantity, the bath temperature (T_C: maximum 45°C) and the required time.

There are three stages in a sample preparation: cleaning of the substrate, preparation of the polymer solution to be deposited, then annealing of the polymer.

Surface treatment is essential for avoiding the presence of impurities on the substrate surface. The slightest impurity can generate a contamination that leads to the separation of deposited layers.

– To clean a silicon substrate, an acetone solution at 30°C is used as the ultrasonic bath. After 15 minutes, the wafer is removed from the bath and abundantly rinsed with distilled water followed by ethanol and finally dried by a flow of pressurized dry air. The wafer is then ready to be used as the substrate for the polymer film.

– For a Cu/Ni alloy, the cleaning is done with acetone and distilled water to prevent damage of the nickel layer.

– Quartz or metal (Al) substrates are submitted to ultrasonic cleaning with distilled water and acetone. Each of these baths is applied for 15 min. The substrate is then dried under a flow of pressurized dry air.

Polymer solutions are prepared using a double-barrel syringe with several spare parts. Before the deposition of polymer solutions, it is cleaned by solvents, such as acetone or ethanol. Polymers are generally provided in liquid form of variable viscosity. When the polymer is composed of two components, namely a resin referred to as R and a catalyst referred to as C, R and C must be mixed in a proportion according to the provider specifications (1:1 or 10:1). Since the mixture must be homogeneous, a magnetic stirrer is used for 2 min at 200 rpm for the mixing. Then, several drops are deposited on the substrate using a measuring syringe, before starting the above-described spin-coating process. Programming of the processing steps is set beforehand, depending on the calibration curve of the device. For current polymers, the standard deposition parameters are 1,500 rpm for 55 s and a start ramp of 55 rpm per second. The same deposition conditions are generally maintained for various preparations. The preparation setup is placed under a 30 mbar vacuum for degassing, to prevent bubble formation. This step is carried at ambient temperature.

The next stage after film formation is the curing at a given temperature depending on the polymer to be cross-linked. The cross-linkage mode and the polymer temperature are found in the provider datasheet. If the provided values are respected, a fully polymerized sample can be obtained. In general, if the recommended temperature is exceeded, the material irreversibly deteriorates. Cross-linkage requires a furnace that can heat up to 2,000°C. A degassing chamber comprising a vane pump for low vacuum prevents in a gray room the presence of ambient impurities in the form of dust or aerosol present in the air.

1.2.2. *Physical method: cathode sputtering*

Cathode sputtering (Figure 1.3) involves the bombardment of a target with an inert gas, argon maintained under a reduced pressure ranging between 5 10^{-1} and 10^{-3} Torr, in order to sputter the atoms in the target. It is a mechanical process that depends on the momentum lost by the collider when the Ar^{+} ion collides with the atom in the bombarded target. This process does not depend on temperature. Applying a potential difference between the target (cathode) and the substrate (anode), the sputtered atoms are accelerated and deposit on the substrate. This technique is also known as “sputtering deposition” adequate for thicknesses below 3 µm.

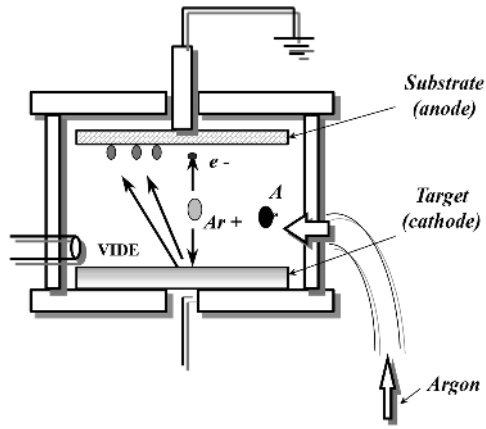

Figure 1.3. *Cathode sputtering. For a color version of this figure, see www.iste.co.uk/dahoo/metrology1.zip*

This technique was used to prepare multi-layers of SiO_2 and TiO_2 films in order to create a 1D magneto-photonic crystal. The target material to be deposited is introduced in a vacuum chamber in the form of a plate of several millimeters thickness and whose dimensions are equal to those of the plate to be coated. This target is fixed at a cathode that is cooled and is maintained under a negative voltage ranging between 3 kV and 5 kV. The anode, which plays the role of the substrate holder, is set in parallel to the target, at a distance of several millimeters. It is generally grounded, for ease of use. For a residual pressure in the chamber maintained between 1 and 10^2 Pa, the electric field between the two electrodes generates the ionization of the visible residual gas in the form of a luminescent plasma cloud. An electric current is then established between the two electrodes, through the conductive plasma formed of electrons, which are attracted by the anode, and positive ions, which are attracted by the target cathode.

A 1D magneto-photonic crystal is a multi-layer stack of a dielectric and a magnetic material characterized by enhanced magneto-photonic properties. The magneto-optical response (Kerr rotation of polarized light) is studied as a function of the thickness of the films by calculation prior to the crystal manufacture and its characterization. The deposition parameters having been calculated, alternating thin films of SiO_2 and TiO_2 are deposited by cathode

sputtering according to the calculated specifications. The criteria to be met are:

– state of the surface: the stacks of dielectric films require the least possible individual roughness of the films to minimize the perturbation generated by this type of defect in the developed structures;

– nature of the material: there should be a significant contrast between the materials to be stacked, with the lowest possible extinction coefficient, which explains the choice of TiO_2 and SiO_2;

– deposition speed: since the development of multilayers requires a significant number of periods, high deposition speeds of single layers are chosen for the stacks over a reasonable period of time;

– deposition temperature: it should be the lowest possible to limit inter-diffusion at the interfaces between SiO_2 and TiO_2 layers.

AFM is used for the study of surface roughness, and ellipsometry is used to determine multilayer thickness and (optical n and k) indices.

The 1D magneto-photonic crystal is thus manufactured using cathode sputtering for multi-layer stacking [HAM 06, HAM 07] and is studied for its properties as smart material at the nanometer scale.

1.2.3. *Physical method: laser ablation*

The principle of thin-film deposition by laser ablation (Pulsed Laser Deposition) involves a nanosecond or femtosecond pulsed laser beam focused on a bulk target (oxide target), in an ultra-high vacuum chamber. The first pulsed laser depositions (PLDs) were conducted in 1965 by Smith and Turner [SMI 65], long before it became widespread, thanks to the development of high-density short-pulse lasers initiated in 1987 [DIJ 87].

The description which is given as an illustration of laser ablation technique concerns the research works conducted at the University of Versailles St Quentin in a laboratory of the National Center for Scientific Research in France for the study of thin films of magnetic oxides of nanometric thickness [DAH 04a, DAH 04, FRA 05, HAM 06, HAM 07, NOU 07]. Two power UV lasers are used: a chemical excimer laser (248 nm) and a solid laser with doubling and tripling crystals. Beyond a certain fluence (amount of energy per unit area or surface energy density),

a light plume can be noted on top of the target. This plume corresponds to a directed expulsion of matter, in the form of a plasma, which can be described as a "gas" of ions, atoms and electrons. These particles are ejected at a high speed while the whole preserves its electrical neutrality. This ejected matter is then collected on a substrate, which is generally a quartz plate located above the target and maintained at a certain deposition temperature. Figure 1.4 shows a schematic representation of the setup corresponding to the laser ablation system.

The samples are prepared in a very high-vacuum chamber under a pressure above 10^{-6} Torr. A light beam from a solid pulsed laser of 10 ns that operates in UV at 385 nm with a repetition rate of 10 Hz is focused on a target that is generally prepared by sintering in the chamber. A reflecting device composed of mirrors that can randomly scan the laser beam on target thanks to an algorithm-based control of the device mirrors is used. The diameter of the laser beam transmitted through a silica window randomly describes a square on the target. Fluence ranges between 2 J/cm^2 and 20 J/cm^2. The substrates (quartz, MgO, etc.) located at the required distance (40 mm to 70 mm) from the target are placed on a holder maintained at an optimal controlled deposition temperature (maximal value of 1,000 ± 5°C) in an oxygen atmosphere under a pressure of up to 500 mTorr.

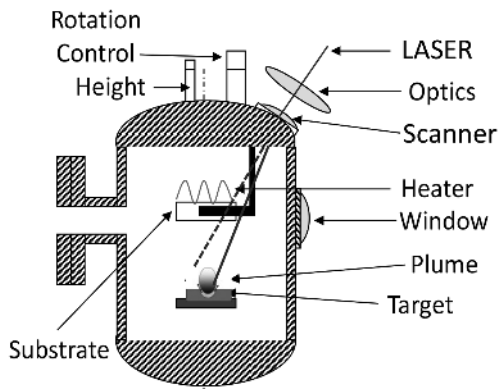

Figure 1.4. *Schematic representation of laser ablation deposition setup. For a color version of this figure, see www.iste.co.uk/dahoo/metrology1.zip*

The solid laser is a flash-pumped Nd: YAG laser. At the output of the laser cavity, a frequency-doubling KDP crystal is used to generate the

second harmonic of laser light at 532 nm. A crystal mixing radiation at 1,064 nm and 532 nm is used to obtain a beam of UV light at 355 nm. Concerning the value of laser radiation fluence at the level of the material, laser radiation–material interaction studies show that it can be classified into three categories:

– Low fluence: the energy deposited by the laser diffuses in the material. It can activate chemical processes at the surface of and/or within the material. The vaporization rate is negligible.

– Intermediate fluence: laser energy is at equilibrium with the losses by heat diffusion and by fusion and vaporization processes. Vaporization is more significant and vapor remains transparent to radiation.

– High fluence: under this regime, a plume appears above the surface of the material, which is generally no longer transparent to laser radiation. Moreover, it may react with the ambient atmosphere and the target material.

The existence of "threshold fluences" beyond which these various phenomena occur can be experimentally observed. They depend on several parameters: radiation wavelength, nature and pressure of the ambient atmosphere and nature and state of the target surface.

A range of parameters can be varied during deposition:

– characteristics of the laser beam: power, beamwidth, duration of the pulse (between 5 and 10 ns for the pulse time at mid-height);

– pressure: between 10^{-4} and 10^{-6} mB;

– temperature of the ceramic heater: between 300 and 800°C;

– oxygen pressure: to maintain the stoichiometry of the sample and confine the plasma. It varies between 60 and 250 mTorr;

– the target–substrate distance: from 40 to 70 mm.

Since the way atoms or molecules are arranged at the surface of a layer determines its morphology and structure, this initial organization plays an essential role in its physical and/or chemical functionalities. Layer growth and morphology optimization is therefore decisive. The growth of layers obtained by laser ablation is achieved by two-dimensional nucleation of aggregates. At a low fluence, these aggregates are small and, in parallel with the subsequent formation of islands, atoms and aggregates scatter at the

surface of the substrate, leading to the formation of layers on top of which aggregates grow. The morphology and structure of layers resulting from this growth mode depend on the conditions of deposition such as the target–substrate geometry, substrate characteristics (surface, nature, temperature), oxygen pressure or the fluence of the ablation laser. Layer growth control involves the optimization of these parameters by in situ controls. As the nature and quality of the deposited layer depend on many parameters (laser energy or fluence, the pressure of the residual gas in the chamber, substrate temperature, etc.), in order to control in situ growth, during deposition, a spectroscopic ellipsometer, as schematically represented in Figure 1.5, was set up in parallel with the preparation system [DAH 03, NOU 07, DAH 11, COA 12]. This non-destructive technique described in Chapter 8 of the [DAH 16] is used to determine layer thickness and optical parameters, i.e. those data required for the analysis of the measurements conducted in magneto-optical spectroscopy.

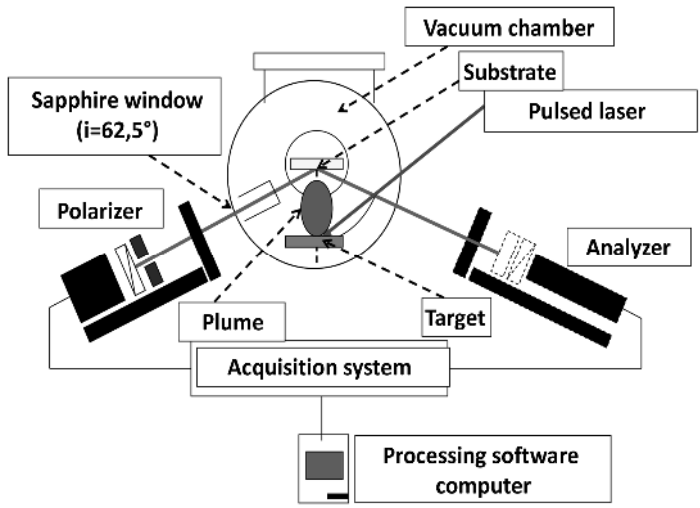

Figure 1.5. *Ellipsometry-based in situ control of thin-film growth. For a color version of this figure, see www.iste.co.uk/dahoo/metrology1.zip*

The results obtained on a thin film of perovskite structure magnetic oxide $SmFeO_3$ deposited on a quartz substrate are given in Figure 1.6(a) and (b) for various temperatures. The ellipsometry parameters cos(Δ) and tan(Ψ) (Chapter 8 of [DAH 16]) are given depending on the wavelength for various temperatures ranging between 300 K and 1,095 K.

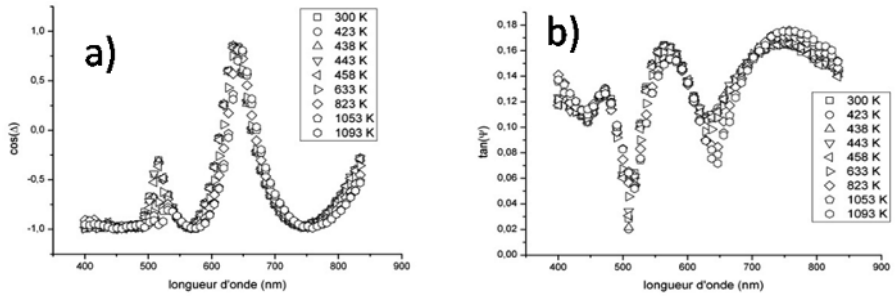

Figure 1.6. *Variation with temperature of a) cos (Δ) and b) tan (Ψ)*

The analysis of the curves shows that beyond 600 nm, cos (Δ) oscillates between ±1, which corresponds to a very low absorption zone. In the absence of thin film, the substrate gives a value of +1 for cos(Δ). When the thin film is deposited, cos(Δ) varies between -1 and +1, the number of oscillations increasing with the thickness of the film. Below 600 nm, in the absorption zone, the maxima remain below 0.1. When temperature increases, varying positions and amplitudes of the extrema can be noted. They shift towards longer wavelengths, which corresponds to an increase in the thickness of the film following the material growth. The amplitudes decrease significantly in the absorption zone, which corresponds to an increase in absorption with temperature. Concerning the parameter tan (Ψ), in the absence of thin film, the quartz substrate gives a ratio of the amplitudes r_p/r_s whose variation is linear in the spectral range from 300 nm to 850 nm, between 0.18 and 0.20. When the film is between the substrate and the air, a variation of tan (Ψ) around this straight line can be noted, with the extrema shifting towards long wavelengths when the thickness increases or the temperature rises. The excursion of the amplitudes, on either side of this line, is a function of thicknesses and absorption.

For the fabrication of a one-dimensional magneto-photonic crystal [HAM 06, HAM 07], the optical properties of TiO_2 and SiO_2 could be determined in the chamber fitted with the ellipsometer, as shown in Figure 1.7. In this case, the target being made of TiO_2, then TiO_2 deposited on SiO_2 could be characterized. The deposition was achieved using an excimer laser that emits a radiation of 248 nm during the discharge triggered by a thyratron in a gaseous mixture of krypton and fluorine. The energy of each pulse, with a duration of about 25 ns, varied over the range from 150 to 650 mJ; fluence

was fixed at 1.8 J/cm^2. Laser repetition rate could be adjusted between 1 Hz and 20 Hz and was fixed at 10 Hz. Substrate temperature was maintained at 300°C, and the pressure of the oxygen in the chamber was measured to be 0.0373 mbar. It is worth noting that laser ablation of SiO_2 at this wavelength is not possible due to an absorption band at 5.01 eV in resonance with the frequency of the excimer laser so that the deposited energy is mainly dissipated by radiative relaxation that manifests as photoluminescence (Figure 6.8 in Chapter 6 of [DAH 16]).

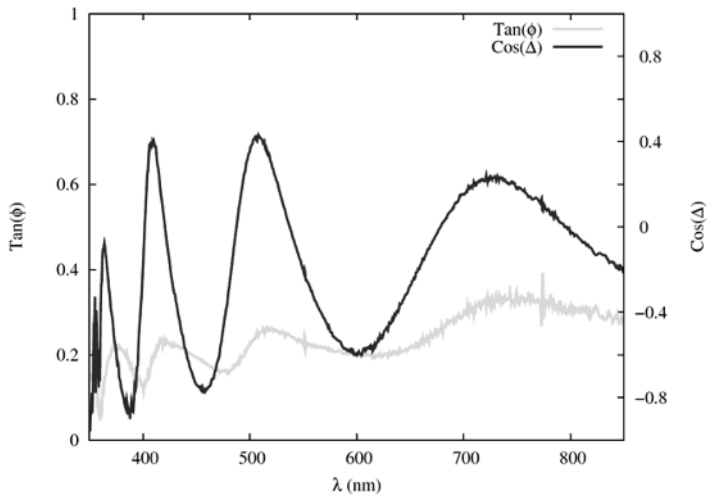

Figure 1.7. *Ellipsometric parameters of a film of TiO_2 on SiO_2 by laser ablation [HAM 07]. For a color version of this figure, see www.iste.co.uk/dahoo/metrology1.zip*

RHEED (reflection high-energy electron diffraction) [RUS 33, COL 72] is generally used as in situ probe to control the growth of thin films. This technique is sensitive to changes at the surface, due to the changes in structure or to adsorption. It involves the bombardment of a target surface with very high-energy electrons. Electrons are then diffracted in various directions with different intensities. The impact of electrons on a phosphor screen gives an image formed of bright spots that correspond to the arrangements of atoms on the surface. A beam of accelerated electrons (5–100 keV) under grazing incidence (0.5 to < 3 deg) is reflected on a surface. Due to their energy, the penetration of electrons is significant. But because of the grazing incidence, only few atom layers are probed. Hence, this technique is sensitive to surfaces.

Two types of diffraction are possible: by reflection and by transmission–reflection: 1) diffusion by a 3D crystal island (image in the upper part of the screen); 2) 2D surface diffusion by a plane surface (image in the lower part of the screen). The energy of electrons in a RHEED experiment may vary between 10 keV and 100 keV, but most of the instruments use energy between 10 keV and 35 keV. Let us recall that 1 eV is the kinetic energy gained by an electron that is accelerated under a potential difference of 1 V. The kinetic energy is $E_c = 1/2\ mv^2$, where v is the speed of the electron and the electric energy is expressed in eV. The speed is $v = \sqrt{(2eV/m)}$ and using the momentum $p = mv$ and the de Broglie relation $p = h/\lambda$, it can be deduced that $\lambda = h/\sqrt{(2meV)} = \lambda_c$ for a non-relativistic electron. Under relativistic conditions, when energies are high, mass correction must be taken into account, and therefore $\lambda = \lambda_c(1/\sqrt{(1 + eV/2mc^2)})$. The corresponding wavelength varies between 0.0037 nm and 0.0146 nm for energies of 100 keV and 10 keV.

1.3. Characterization of samples

A thin film of a given material is an amount of that material having one of its dimensions, referred to as thickness, significantly reduced. This thickness (in nanometers) corresponds to the distance between two boundary surfaces (quasi bi-dimensionality). This 2D structure results in a perturbation of most of its physical properties. The essential difference with the bulk state is that the role played by the boundaries in the bulk properties is generally considered negligible. On the other hand, in a thin film, the effects related to boundary surfaces are predominant. The smaller the thickness, the more pronounced is this bi-dimensionality effect. Conversely, beyond a certain threshold, the effect of thickness becomes negligible and the material regains its properties of the bulk material. Any method of analysis requires a probe (electromagnetic radiation, a beam of energetic particles, a field, a mechanical penetrator, etc.) acting on a sample. The result of the interaction between this probe and the sample can be another radiation, particles, field variation, detected by a chain of measurement or by a behavior law.

To observe small-sized objects, a microscope equipped with lenses is used in order to realize a magnification of the object when it is viewed through the objective of the apparatus. The object must be illuminated, which is done either by reflection or by transmission, the light reflected or scattered by the object being then recovered by the objective, which forms

an image that can be observed. It is in 1873 that E. Abbe [ABB 73] formulated his mathematical theory concerning images formed by a microscope and showed that a point could not be imaged by a point. While working on the theory, he identified a limit to the size of the observable object, which was due to the resolution $d = 0.61\lambda/ NA$, where the numerical aperture is $NA = 2n\sin\alpha$. It is expressed as a function of the maximal angle α between the optical axis and the rays coming from the object viewed through the objective under which various rays lead to the formation of the image of the object; n is the refractive index of the environment in which the object is immersed. This resolution limit is nowadays known as the Rayleigh criterion and is associated with the wavelength λ of the radiation used for the observation. It is due to interference effects that lead to the formation of the Airy disk, which for an aperture of diameter D is given by $1.22\lambda/D$ under incoherent illumination. The same phenomenon accounts for the "waist" present in the Fabry–Pérot setup used in a laser device, as described in Chapter 6 of [DAH 16] (Figure 6.2). Resolution is limited to 200 nm in the visible spectrum. Abbe thought however that this limit could be overcome with the forthcoming progress in the understanding of physical phenomena or technology.

Indeed, around 55 years later, in 1928, E.H. Synge [SYN 28] proposed a thought experiment that laid the bases of near-field microscopy of modern optics, considering that it was possible to obtain resolutions beyond the limits imposed by diffraction. He considered that it was possible to observe by transmission the interaction of light and matter between an object and the light that would reach the object through a small aperture of dimensions smaller than the wavelength, of the order of 50 nm to 100 nm, in a screen that scans the surface of the object, as shown in Figure 1.8. Using this method, the limit of resolution is no longer imposed by the wavelength, but by the aperture through which light passes. In the theory of light diffraction through a small aperture, the components of the far field can propagate, while in the near field, they are evanescent (see the Appendix: Propagation of a Light Ray). In the proximity of the object, spatial frequencies are high. Referring to the works of Fresnel and to Babinet's theorem, a small-size aperture being equivalent to an object of the same dimension from the perspective of diffraction, this principle prefigures the use of a tip to probe the evanescent waves near a surface.

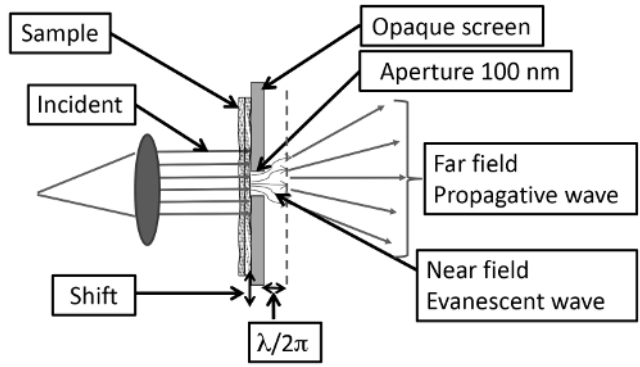

Figure 1.8. *E.H. Synge experimental setup. For a color version of this figure, see www.iste.co.uk/dahoo/metrology1.zip*

Similar to nanotechnologies, it took a while for the idea to be put into practice. In this case, four decades were needed to obtain a better resolution with a scanning microscope developed in 1972 [ASH 72], in the domain of microwaves with a wavelength of 3 cm. A grating could be resolved with a resolution of $\lambda/60$ by this technique.

But meanwhile, scanning tunneling microscope (STM) was invented by Binnig and Roher in 1981 [BIN 82a, BIN 82b, BIN 83, BIN 86a]. The operating principle of STM, which uses the scanning method, relies on the possibility to establish a tunneling current between a metal tip and a metal or conductive surface when a potential difference is maintained between the tip and the surface. The intensity of this current depends on the distance between the tip and the surface. When the tip scans the surface, there is a variation of the distance between the surface and the tip due to surface topology, and consequently the tunnel current, which depends on this distance, also varies. In this case, the current variation is a measure of the surface topology. A second operating mode involves maintaining a constant distance between the surface and the tip. Taking a starting point as a reference, a rated current is fixed. Given that the current variation is positive when the distance between the tip and the surface decreases, and that it is negative when the distance increases, this variation is injected into a feedback system (negative feedback loop) in order to maintain a distance that is equal to the reference distance. The positive or negative correction of the position, made by moving the tip using a piezoelectric system [SYN 32] that expands or contracts when subjected to a potential difference (see Chapter 7 on

intelligent materials), is in this case directly related to the topography of the surface. It is worth noting that nowadays STM belongs to the class known as scanning probe microscopy (SPM), but its use is limited to electrically conductive materials.

Finally, in 1984, the first near-field optical microscope is developed [POH 84] in the visible spectrum. The operating principle of scanning near-field optical microscope (SNOM) or near-field optical scanning microscope (NSOM) relies on the Synge principle, but uses an STM, with a probe instead of an opaque screen with an aperture, that is localized in the near-field zone. At nanometric distances, the movement of the probe on a surface is in fact easier to control than that of an opaque plate with an aperture.

A brief description of a SNOM by transmission is provided, as schematically represented in Figures 1.9. and 1.10, highlighting the main elements required for its operation. In a typical optical setup, a laser beam, after passing through neutral filters, is collimated, so that the light rays are quasi-parallel, which corresponds to the propagation of a plane wave (Figure 6.2, Chapter 6 of [DAH 16]). It is then directed under the acceptance angle in an optical fiber whose tip end is near the surface to be analyzed. An optical system is used to recover the signals collected in near field on an APD (Avalanche Photo diode) detector for an analysis through a spectrometer and a processing software. The main elements contributing to data collection are the tip-shaped probe and the precise measurement of the probe movement with respect to the sample by means of a piezoelectric plate subjected to a potential difference. The latter which drives the tip along X, Y or Z is a function of the error signal generated by the laser detection system with a PSD (Position Sensitive Detector) quadrant, which gives the tip position with respect to the surface during the lateral scanning generated by the piezo stage. This scanning is in raster mode, similar to the scanning mode on a television screen. The feedback loop system operates in two modes: at constant force or at shearing force.

In Figure 1.9, the setup of the piezo stage corresponds to the constant force mode. In this case, scanning can be conducted in 3 modes. The contact mode corresponds to the situation in which the tip touches the surface of the sample and maps the topography of the surface. In this mode, there is a risk of sample damage. The tapping mode corresponds to a flexible tip that undergoes deflection according to the topography of the surface. The laser-PSD system measures the deflection angle and generates an error

signal, which is used to activate the piezo stage by the feedback loop in order to bring the surface to the reference nominal distance. Finally, the non-contact mode corresponds to that of a high-frequency generator being associated with the tip under oscillation. The amplitudes of these oscillations are modified according to the topography of the surface, and depending on whether the surface gets closer or farther, the vibrations are damped or relaxed by long-range (dispersion) forces between the surface and the tip. Depending on the decrease or increase in vibration amplitudes, the feedback system modifies the distance between the tip and the surface.

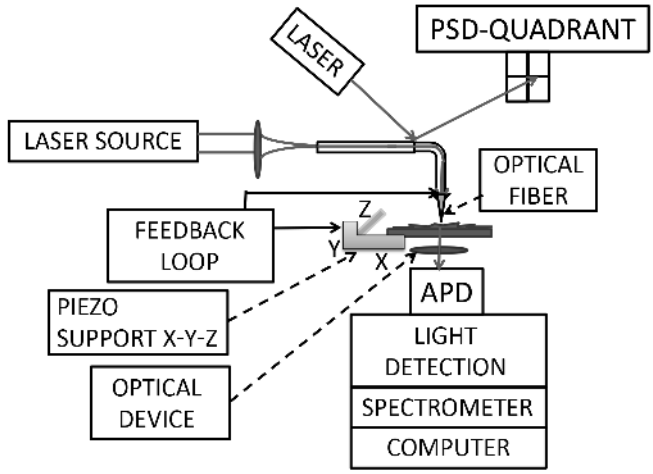

Figure 1.9. *Diagram of a SNOM by transmission in constant force mode. For a color version of this figure, see www.iste.co.uk/dahoo/metrology1.zip*

Another possible setup is that of the tip-carrying fiber being attached to a tuning fork, which sets the tip in a lateral vibration movement above the surface (Figure 1.10). In this shearing force mode, the positioning principle is similar to the above-described contactless mode. Hence, similar to an STM that gives the possibility to probe the metallic surfaces at nanometer scale, the near-field optical microscopy can be used to reach sub-wavelength resolution. A local probe detects a non-radiative signal confined in the close vicinity of the surface, similar to the tunnel current, which is active on the sample surface. Since the probe scans the sample surface at a distance or height of several nanometers, similar to the STM, a negative feedback loop is used to follow the topography of the surface.

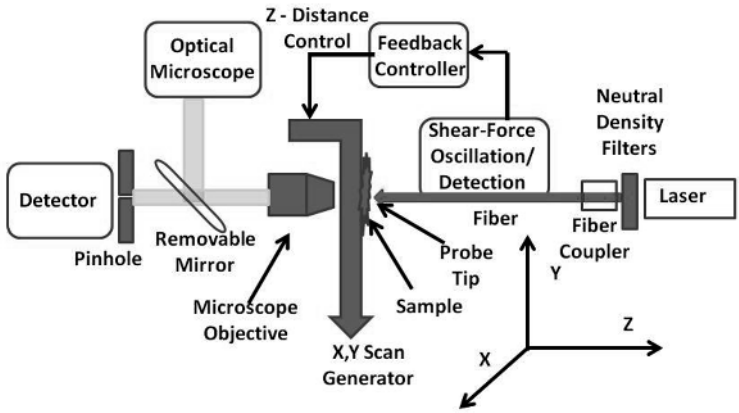

Figure 1.10. *Diagram of transmission SNOM in shear mode. For a color version of this figure, see www.iste.co.uk/dahoo/metrology1.zip*

The atomic force microscope (AFM) was invented in 1986 by Binning, Quate and Gerber [BIN 86b] in a collaboration between IBM and Stanford University. A more detailed discussion on the use of this instrument is provided in the study of thin films of magnetic oxides prepared by laser ablation in section 1.3.2.

In summary, the types of microscopes commonly used nowadays correspond to tunneling and atomic force near-field microscopes, referred to as STM and AFM, respectively. The very high spatial resolution characterizing near-field techniques is related to the very small size of the probe – in the two cases considered, the nanometric apex of a conductive or semi-conductive metallic tip brought to near-contact (a fraction of nanometer) with the surface of the sample. These microscopes use the localized interactions of the tip with the sample and their rapid variation of intensity with the probe–sample distance: the passage of the tunneling current for the STM from which a mapping of the surface atoms is obtained through their local electronic density, and the forces acting on the tip (e.g. Van der Waals interactions for the AFM).

These near-field microscopies give also access to further information, such as electronic spectroscopy by STM and mapping of force fields for AFM and its homologues. The downside of the spatial resolution of these microscopies is the limitation of the analysis to the surface of the sample and

to the zones of limited dimension, STM use being also limited to the study of conductive samples. Moreover, the probe may have an invasive effect.

It is worth noting that optical microscopy in the context of light–matter interaction can also be implemented in far field, being in fact less invasive and making it possible to observe (imaging, localization, detection) the sample. Moreover, many spectroscopic signatures can be studied through various spectroscopies using a classical source or a laser as source (Chapter 6, [DAH 16]) such as Brillouin or Rayleigh scattering, absorption or emission spectroscopy (fluorescence or phosphorescence) or Raman spectroscopy, the pump-probe spectroscopy, the double resonance used for probing the properties of matter through the various sub-structures of its energy levels. This spectroscopic analysis can be further extended to the acquisition of physical and chemical parameters such as the lifetime of electronic states. The reader who is interested in the developments of these techniques can refer to the list of references [LEW 833, BET 86, BET 87, FIS 88, COU 89, RED 89].

1.3.1. *Scanning electron microscope*

Electron microscopes are based on the wave–particle duality of the electron Reducing the wavelength of the radiation provides a better resolution than conventional optical microscope. Historically, the first revolution in the field of very high-resolution imaging is that of scanning and transmission electron microscopies (SEM and TEM) (RUSKA 1931), which provide images with nanometer and even atomic resolution due to the nanometer dimension of the electron beam for SEM. Electron microscopy is a very powerful tool, which can also be coupled with spectroscopic chemical analyzes (EELS: electron energy loss spectroscopy) in TEM and structural (diffraction) but their implementation remains very limited, and Electron microscopy is also now widely and mainly used as an imaging tool.

The scanning electron microscope (SEM) relies on the wave properties of an electron to obtain magnification. Figure 1.11 shows the schematic representation of an electron microscope in TEM and SEM modes.

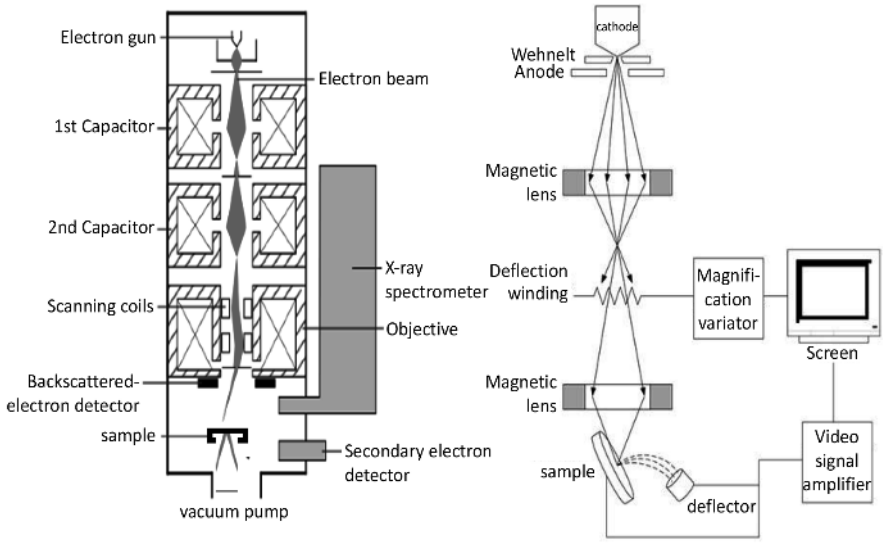

Figure 1.11. *Electron microscope: TEM and MEB modes. For a color version of this figure, see www.iste.co.uk/dahoo/metrology1.zip*

A beam of mono-kinetic electrons is produced by a tungsten filament through which a current is generated by the thermionic effect. Electrons are accelerated by a potential difference V of the order of 100 keV. The wavelength λ associated with electrons is given by the de Broglie relation, $\lambda = h/(\sqrt{2m_e eV})$, where m_e designates the mass of the electron and e its charge. Under 100 keV, the electron wavelength λ is 0.0037 nm. This beam is directed and focused by magnetic lenses to obtain a very small-diameter probe (about 0.01 μm) that scans the surface of the studied sample. Because electrons penetrate the material, the resolution is however not good (rather of the order of a micron for backscattered electrons and of the order of several tenths of a micron for secondary electrons). Electron scattering through the studied sample can be either elastic (no energy loss upon interaction with the nucleus and electrons inside the atoms), which leads to diffraction or plastic (effect of heterogeneities such as grain material boundaries, dislocations, defects, density variations, etc.), which leads to a variation in the intensity of the transmitted beam. The two modes of operation of a TEM are the image mode and the diffraction mode.

The interaction between the beam of electrons and the material generates various types of radiation:

– backscattered electrons;

– secondary electrons;

– absorption generating a current in the sample;

– Auger electrons related to atom de-excitation;

– X-rays emitted during de-excitation following the ionization of electron shells inside the atoms.

The studies of thin films of magnetic oxides were conducted with a Philips CM20 TEM and a Jeol 200CX TEM operating at 200 kV. The two instruments were equipped with a sample support that could be tilted along two axes. Adjustments were directly made on the image displayed by the screen of the image intensifier. Sample preparation involves thin-film manufacturing by ion bombardment perpendicular to the surface (section of the plates). Due to the ion tendency to melt the material, a proper control of this stage is required to avoid sample damage. For the analysis of sections, the surfaces of two pieces of epitaxial layers are glued with epoxy. The section is then mechanically polished on both sides until reaching a thickness of 30 μm and then carefully thinned down by a flow of low-speed argon ions on the samples (6 kV and 10 mA) on a liquid nitrogen-cooled support. This process prevents damages. A surface of the order of 20 μm^2 can then be analyzed by TEM [DAH 04a]. Figures 1.12(a) and (b) and 1.13(a) and (b) show images obtained by TEM for $SmFeO_3$ materials deposited at 785°C and 820°C, respectively.

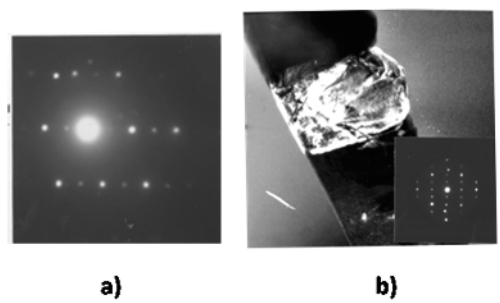

Figure 1.12. *Diffraction images obtained by TEM for SmFeO3 samples deposited at: a) 785°C and b) 820°C*

TEM-based diffraction analysis reveals two types of structures depending on the temperature deposition of the $SmFeO_3$ film on a quartz substrate: a cubic structure (Figure 1.13(a)) and an orthorhombic structure (Figure 1.13(b)). The deposition has a columnar form in volume with surface extrusions, as shown in Figure 1.12(b) and Figure 1.13(a) and (b).

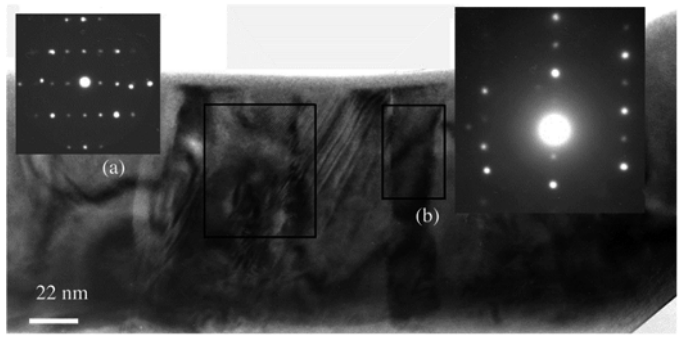

Figure 1.13. *TEM diffraction images for SmFeO3 films deposited at: a) 785°C and b) 820°C*

Figure 1.14(a) and (b) displays SEM images of $SmFeO_3$ films deposited on a quartz substrate at a temperature of 915 C. It is worth noting the presence of protuberances whose dimensions range between 150 and 500 nm, as observed in TEM, and cracks due to different expansion coefficients of the substrate and of the oxide layer, ranging between 50 and 90 nm.

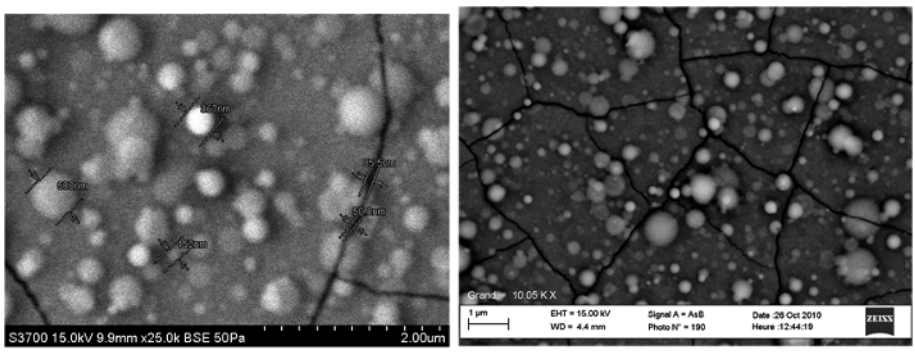

a) (b)

Figure 1.14. *SmFeO film deposited at TD = 915°C: a) protuberances between 150 and 500 nm; b) cracks between 50 and 90 nm*

1.3.2. *Atomic force microscope*

The atomic force microscope (AFM) is used to obtain three-dimensional analyses of layer roughness with a good vertical resolution. Its operating principle is represented in Figure 1.15 and involves the measurement of the variations of forces of interaction between a tip and the surface under study.

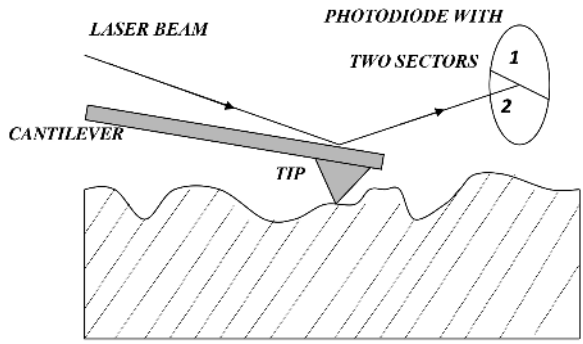

Figure 1.15. *AFM operating principle*

An atomic force microscope is constituted of a piezoelectric quartz plate on which the sample to be studied is placed. The quartz plate lies on an "elevator" engine, and above the sample, there is a very hard tip (read head) fixed at the end of a beam in a frame. A laser beam is reflected on the tip and illuminates two photodiodes. The tip tilt on the scanned surface is determined by the difference in light intensity on the photodiodes. The variation of this electrical signal when the plate under the tip is under translational motion is processed by a software that consequently deduces the topography of the scanned surface.

Figure 1.16 shows the various constituents of an AFM microscope:

– The tip: made from silicon nitride, it is the finest possible, with a pyramid shape.

– The engine: its main role is to lift the sample towards the tip.

– The quartz: it is first of all used for the precise adjustment of the tip on the deposition. Due to the voltage across it (due to the crushing of the tip), it can be used for the computer representation of the deposition surface. Two other voltages are applied to it in order to move the sample in the two directions of the plane.

– The laser: it has a low power – its maximal power is 5 mW. Its essential characteristic is the beam fineness. It emits light in the red band with a wavelength of 670 nm.

– The photodiodes: they generate an electrical signal that is proportional to their respective illumination and thus serve as "sensor of approach" of the tip to the deposit.

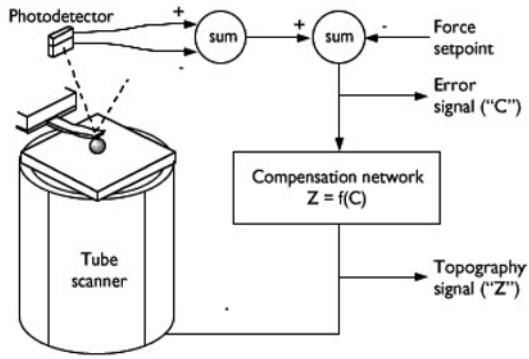

Figure 1.16. *Atomic force microscope*

The work is conducted in the contact mode, the forces being measured in the short range "repulsive" mode.

The laser beam is directed to a metallized part of the cantilever that scans the sample surface horizontally. Due to the deflection of the cantilever, the forces between the tip and the surface can be obtained by the deviation of a laser beam reflected on the metallized part of the cantilever and measured by a quadrant diode (1 and 2). The position of the sample is adjusted along the vertical axis depending on the signal on the diode. Prior to starting a measurement, the laser beam illuminates each quadrant with the same intensity (Itot = I1 - I2 = 0). A vertical variation of the tip position leads to a shift of the beam on the detector and the appearance of the measurement signal (Itot $\neq$ 0). The signal Itot is then used to vary the position of the piezo-electric engine in order to bring the cantilever to the initial position (Itot = 0). The recorded scanning traces are processed and transformed by a special software into three-dimensional images representing the studied surface.

There are several artifacts for surface measurement with AFM. The most inconvenient in the case of thin films are real geometry and the radius of curvature of the tip, as well as the inertia of the feedback of the piezo-electric engine in case of very high roughness. Since a measurement is the result of a convolution between the geometry of the tip and the irregularities of the surface, the shape of the grains observed on an AFM image is not always actual. To avoid the effect of this artifact, scanning under several angles is recommended. The lateral resolution of an AFM image depends on several factors, among which is the morphology of the surface (notably the size of the grains, their amount and the distance between neighboring grains) and the radius of curvature r_c of a tip. For the tip with r_c = 50 nm, the lateral resolution for two grains of height 20 nm is 38 nm. This means that, in order to optically resolve these two grains, the distance between them should be greater than or equal to 38 nm.

The algorithm analyzing the roughness of the film surface is the following: first, a scanning of the maximal possible surface (10 × 10 μm) is conducted, then, if needed, a zone without large grains or agglomerates (scanning surface typically 800 × 800 nm) is chosen and roughness is studied. After having repeated this process several times on different areas of a layer, the mean value of the roughness and the mean size of the grains for polycrystalline layers are obtained.

Images of 2 × 2 μm surfaces on samples deposited under an oxygen pressure of 50 mTorr are displayed in Figure 1.17(a)–(c). Disk- or square-shaped islands of spherical, cylindrical or cubic morphology are observed below the layers deposited at 510°C, 635°C and 755°C. Inspection shows that the size of these islands is smaller at 755°C. The roughness determined on the surfaces of 2 × 2 μm and 10 × 10 μm surfaces is in agreement with the roughness obtained by TEM and SE (spectroscopic ellipsometry) [DAH 04a]. The analysis of AFM images of the samples deposited under three different oxygen pressures (24 mTorr, 52 mTorr and 62 mTorr) are displayed in Figure 1.18(a)–(c), for a temperature of deposition of 920°C. Islands of various forms are also observed, their size being smaller when the pressure is lower. Roughness values between 10 and 30 nm are compared to those determined by TEM and SE [DAH 04a].

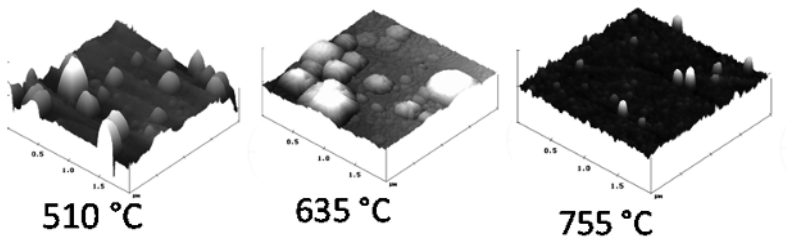

Figure 1.17. *Topology of the deposition surfaces of $SmFeO_3$ on quartz (P = 50 mTorr) for various deposition temperatures. For a color version of this figure, see www.iste.co.uk/dahoo/metrology1.zip*

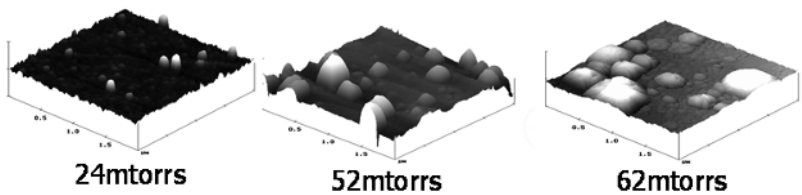

Figure 1.18. *Topology of deposition surfaces of $SmFeO_3$ on quartz (T = 920°C) for various oxygen pressures. For a color version of this figure, see www.iste.co.uk/dahoo/metrology1.zip*

1.3.3. *Infrared spectroscopy (FTIR/ATR)*

Infrared spectroscopy is used to study the vibrational and rotational motions of molecules in the gaseous phase [DAH 17, DAH 19, DAH 21] and also the vibrational motion of molecules in the condensed phase. Modern characterization instruments rely on the principle of spectroscopic interferometry. It is a non-destructive technique. It can be applied to study the vibration modes of molecules in the medium-infrared-energy domain of polymer materials prepared by spin coating. The identified modes of vibration are used to determine the nature of the chemical bonds susceptible to be present in the molecule. The position (wavelength) and intensity (% in height or surface of the rays) of absorption peaks are specific for various chemical groups. The medium-infrared domain corresponds to the interval 400 cm^{-1} < σ (wave number) < 4,000 cm^{-1}.

The general principle of FTIR spectroscopy is presented in Figure 1.19. The infrared beam coming from the source is directed towards a Michelson interferometer that modulates each wavelength of the beam at a frequency that differs from the frequency associated with IR radiation. In the interferometer, light falls on the lens that splits the beam in two. Half of the beam is directed to a fixed mirror, while the rest is directed to a mobile mirror whose movement modulates the IR beam. When the two beams recombine, destructive or constructive interferences occur, depending on the position of the mobile mirror.

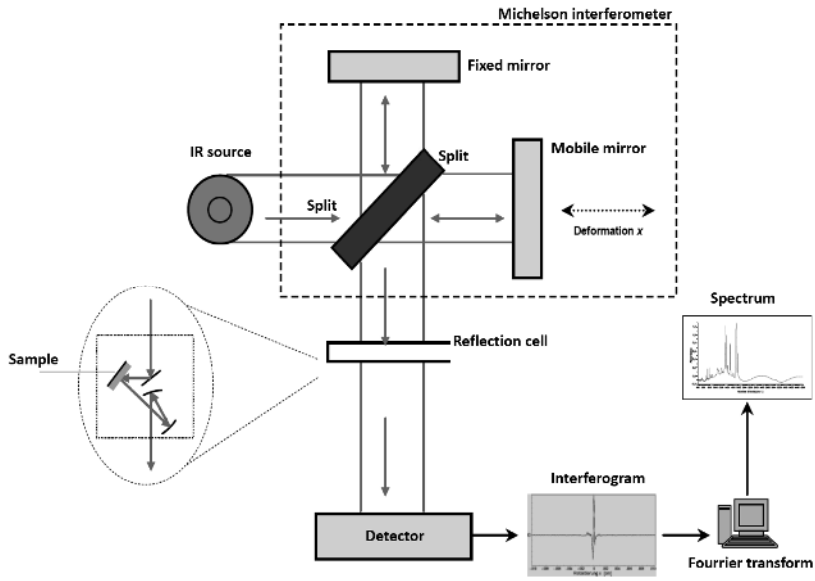

Figure 1.19. *Principle of FTIR spectroscopy, and the cell of measurement in ATR. For a color version of this figure, see www.iste.co.uk/dahoo/metrology1.zip*

The modulated beam is directed towards the sample through a high-index crystal. Absorptions occur in the material in contact with the crystal following an internal reflection and a tunnel effect at the reflection surface. After reflection, the beam returns to a sensor that emits an electrical signal. The latter appears as an interferogram, which is a signal whose amplitude depends on the position of the mobile mirror. This position is determined from a starting position corresponding to an identical position of the two mirrors on the two arms and which corresponds to a zero-path difference

between the two beams and the interference fringes obtained with a He–Ne laser beam that travels along the same path. The modulation of the IR signal corresponds to the Fourier transform of the IR spectrum.

ATR (Attenuated Total Reflection) is a technique that is adapted to the infrared spectroscopy study of materials that are too absorbing or too thick to be analyzed by transmission. In ATR spectrometry, the sample to be analyzed, in liquid or solid state, in the form of powder or thin film, is maintained against the basis of a crystal with high refractive index n_1. For powders and solid materials, a small press is used to maintain the contact with the crystal lens. The other types of samples must be flat or elastic in order to best fit the shape of the crystal.

If n_2 is the refractive index of the sample, there is a total reflection of the incident ray if the angle θ between the sample–crystal interface and the crystal facets is greater than the critical angle θ_c given by the relation: $\sin \theta_c = n_2/n_1$. A certain penetration of the infrared beam takes place at the surface of the sample leading to a decrease in the intensity of the reflected beam in the ranges of frequency where the sample features an absorption. The refractive indices of ATR crystals normally range between 2.4 (ZnSe, KRS-5: mixed crystals of thallium bromides and iodides) and 4 (Ge), and the incidence angles of the systems are generally 30°, 45° and 60°. The total optical path depends on the number of internal reflections, which in turn depends on crystal geometry: length, thickness and angle of incidence.

Using a Thermo Scientific Nicolet iS10 FTIR spectrometer with a Thermo Scientific Smart iTR attenuated total reflectance (ATR) sampling accessory, samples are characterized [KHE 14]. The results in Figure 1.20 correspond to the measurements in the spectral region between 500 and 4,000 cm^{-1} with a resolution of 1 cm^{-1} on various solutions studied in [KHE 14] and whose ellipsometry studies are presented in Chapter 8 of [DAH 16].

The same peaks are found on the spectra of all polymers. The valence vibrations of methyl groups are observed for the CH stretching mode in the form of a group of about 2,962 cm^{-1} and 2,904 cm^{-1}; the stretching vibrations are about 1,413 cm^{-1} followed by a small band at 14,40 cm^{-1}. The antisymmetric stretching of siloxane Si–O–Si functions, which have the

form of a high peak with a shoulder, is about 1,008 cm^{-1} and 1,082 cm^{-1}. Si–C valence vibrations have the form of a very high peak about 784 cm^{-1} corresponding to the rocking stretching of $Si–CH_3$, a stretching mode at 864 cm^{-1} and a significant band at 1,258 cm^{-1} corresponding to a stretching vibration. The seven samples from different suppliers have the same spectral signature, the only difference being absorption intensities and an additional band for M2. The difference in intensity between the absorption peaks reflects a difference in the concentration of functional groups specific to each supplier in the polymer chain.

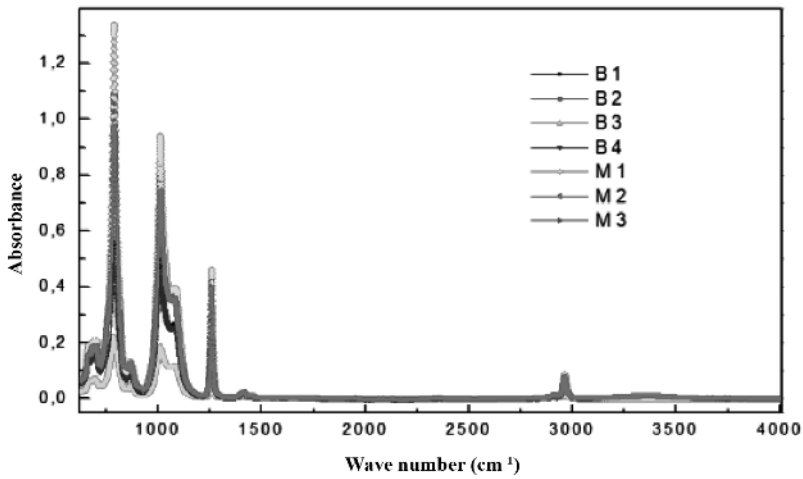

Figure 1.20. *Absorption spectra of silicone gels B (1–4) and M (1–3). For a color version of this figure, see www.iste.co.uk/dahoo/metrology1.zip*

An ATR spectroscopy study of polymers is conducted on samples of polymer subjected to constraints of temperatures and humidity in a super-Highly Accelerated Life Test (HALT) and Highly Accelerated Testing (HAT) device described in Chapter 1 of [POU 20]. Among the characteristics of HALT, which comprises a generator of vibrations and thermal shocks, the following can be listed: a T° slope of 60°/mn, a range of T° between +200° and -100°C and a range of vibration per pistons under the lower plate between 0 and 50 g. The humidity generator can reach a maximal relative humidity of 98%, for a volume of 1,680 liters. To run the aging tests, the test profile software control in terms of temperature, vibration and humidity is activated. The polymer samples were subjected to cycles such as those represented in Figures 1.20 and 1.21.

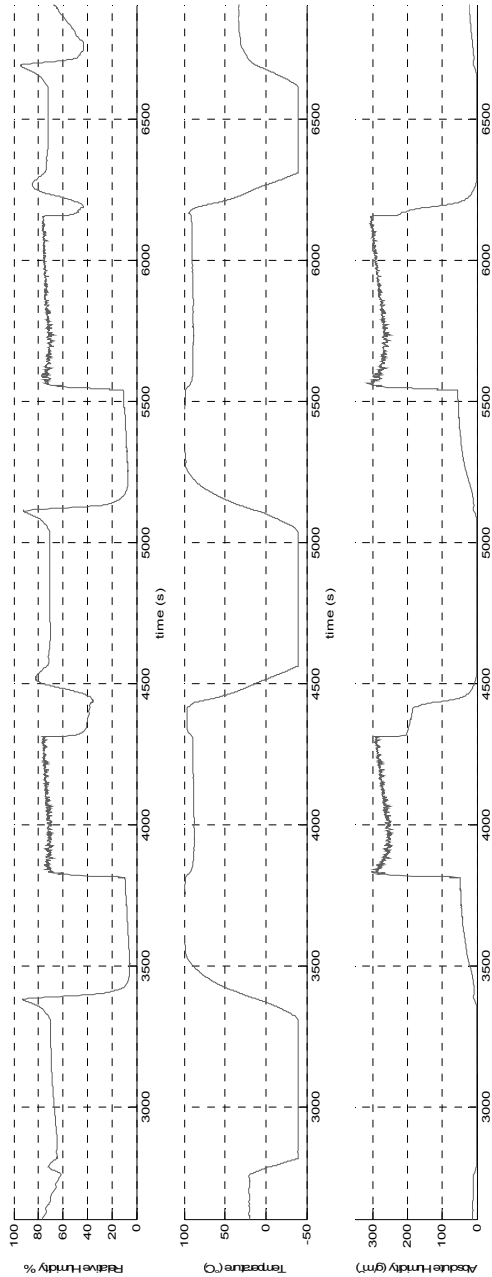

Figure 1.21. *Combined thermal cycling (T: -45 at 95°C) and humidity cycling (HR: 70%) in the super-HAT. For a color version of this figure, see www.iste.co.uk/dahoo/metrology1.zip*

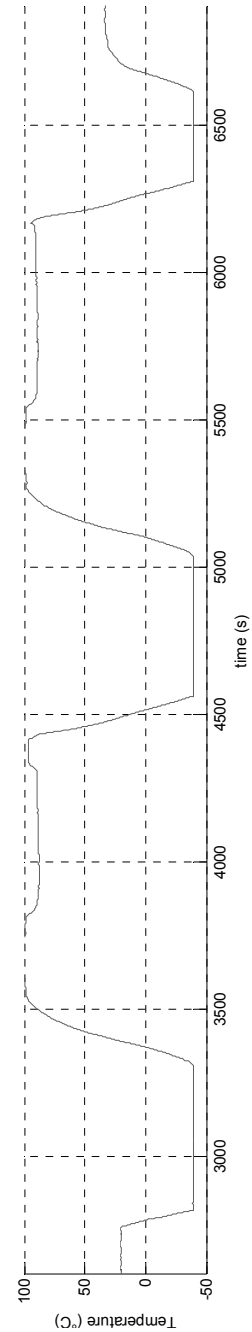

Figure 1.22. *Thermal cycling (T: -45 at 95°C) in HALT. For a color version of this figure, see www.iste.co.uk/dahoo/metrology1.zip*

To study the effect on aging of an environment combining relative humidity with temperature, two types of loads are applied: a (T+H) load (Figure 1.21) combining a temperature cycle (variation of temperature between 45°C and 95°C) with a humid atmosphere (maximum relative humidity rate is 78%) and a (THalt) load consisting of thermal cycles (Figure 1.22).

Another type of aging due to a more classical aggressive thermal stress is conducted on polymers in a furnace. The various stress temperatures are 150°C, 180°C and 200°C. The monitored thermal profile is programmed by a progressive increase in temperature from 25°C to the temperature to be reached during 15 minutes followed by a plateau of 2 h at this temperature. All the samples are subjected to the same process under the same conditions. Figure 1.23 displays the applied thermal cycles.

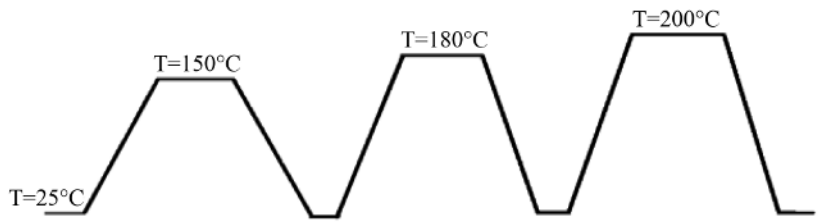

Figure 1.23. *Thermal cycling in a furnace*

The spectra were obtained by ATR in the interval between 600 cm^{-1} and 4,000 cm^{-1}. The analyses show a differentiation in the results in two different spectral regions located between 600 cm^{-1} and 1,500 cm^{-1} and between 2,280 cm^{-1} and 2,400 cm^{-1}. The first interval corresponds to the region of Si–O vibration modes and the second interval to the spectral signature of CO_2 vibration modes, indicating the presence of this molecule that is trapped in nanocages in the polymer structure.

Figure 1.24 shows the spectra obtained with M-type polymers (1 component). Figure 1.25 shows the spectra obtained with B-type polymers (2 components) in the region of Si–O, between 600 cm^{-1} and 1,500 cm^{-1}. The spectra are denoted by {TF} for the thermal stress applied in a furnace, {Thalt} for the thermal stress in a dry environment and {T+H} for the thermal stress in a humid environment.

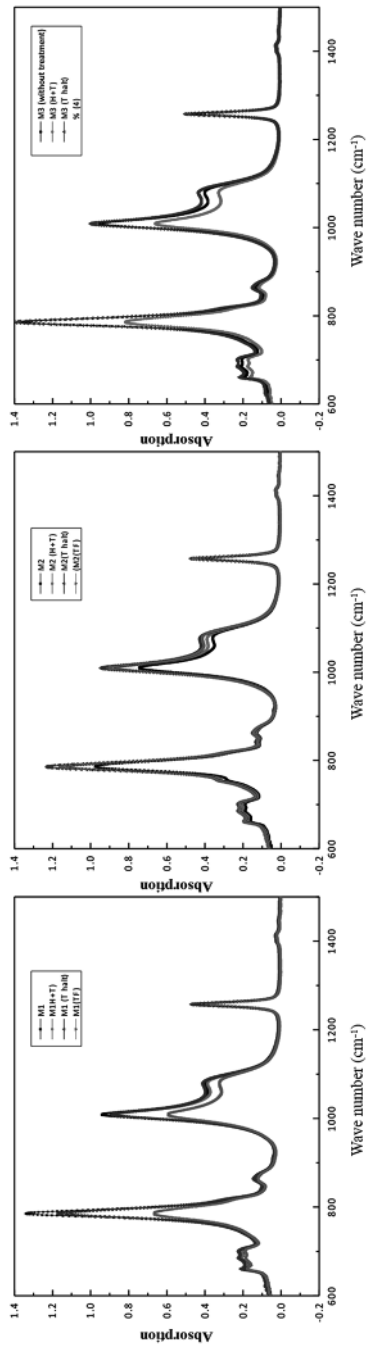

Figure 1.24. *ATR spectra of M-type polymers. For a color version of this figure, see www.iste.co.uk/dahoo/metrology1.zip*

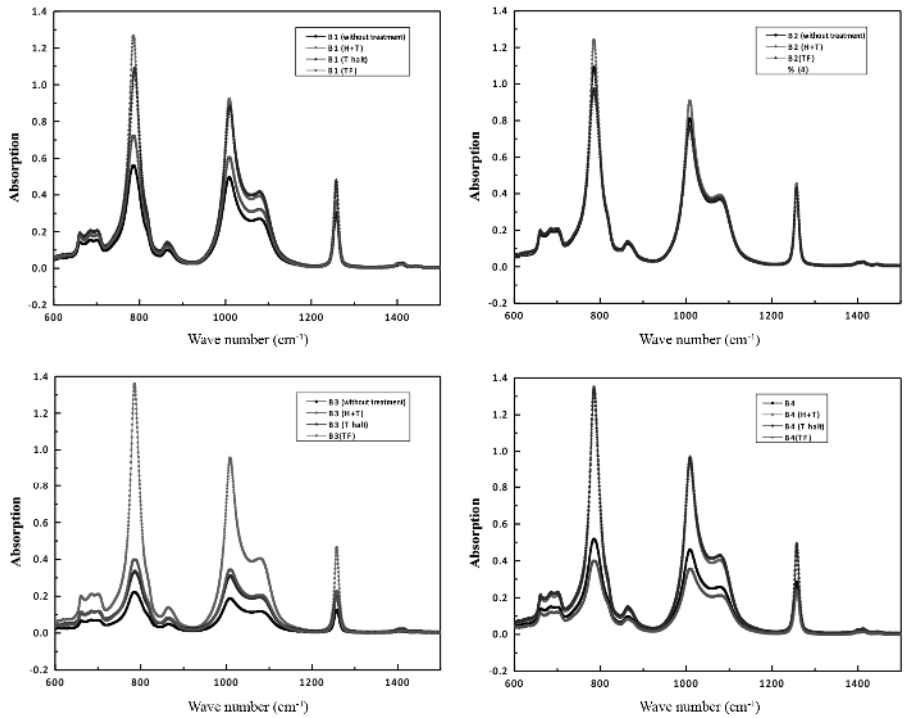

Figure 1.25. *ATR spectra of B-type polymers. For a color version of this figure, see www.iste.co.uk/dahoo/metrology1.zip*

The intensities of absorption peaks vary for each material, but in different proportions. The absorption increases or decreases depending on the material and the TF, THalt or {T+H} loads. As a general rule, the increase or decrease in the intensity of an absorption peak by thermal processing influences also all the peaks of the spectrum in the same direction of variation. Either an increase or a decrease in the intensity can be observed throughout the spectrum, but observing a decreasing peak and an increasing peak and vice versa is excluded. No general tendency of evolution of the intensities of absorptions depending on the thermal processing can be globally established.

The effect on the spectral signatures of {THalt} and {T+H} loads is more or less similar in the two groups of M-type or B-type polymers. In the B-types, the peaks are rather more intense or of the same order as for the M-type. Comparing the effect of the three thermal processes, the spectral signature of the TF effect corresponds to signals of lower intensity than for {THalt} and {T+H,} effects, with the exception of the two compounds M2 and B2 with equivalent signatures.

Concerning the zone located in the region of intense absorption of the antisymmetric stretching vibration of CO_2, between 2,280 cm^{-1} and 2,400 cm^{-1}, the absorption spectra have the same evolutions in the intensities of the peaks of absorptions before and after processing, independently of each material. This analysis yields different results from those obtained on the spectra from 600 cm^{-1} to 1,500 cm^{-1}. Relying on the intensity of absorption bands centered at 2,350 cm^{-1}, the following characteristics are listed.

All the polymers feature a quasi-null absorption in the IR spectrum at a very low level (Absorbance $\approx$ 0) before the application of the thermal constraint. On the other hand, the thermal load in a humid environment {T+H} leads to an increase in absorbance, contrary to the {THalt} and {TF} loads that lead to a decrease in absorbance (Absorbance < 0).

A study of possible absorptions in this region reveals the absorption by triple bonds (C≡O, C≡N) from 2,000 cm^{-1} to 2,500 cm^{-1}, by double bonds (C=O, C=N and C=C) from 2,000 cm^{-1} to 1,500 cm^{-1} and more specifically, the case of a double bond (O=C=O) as in CO_2. For the latter, it is worth noting the presence of a vibration–rotation band (Branch P and R) centered in the gaseous phase at 2,349.14 cm^{-1} due to the absorption of the mode of vibration ν_3 of antisymmetric stretch of CO_2. This corresponds with the identified zone taking into account the effect of nanocage perturbation [DAH 99, DAH 06] on the motion of the molecule as a result of the interaction with the electrical field present in the polymer. In order to evidence the presence of CO_2 in the polymers, the difference spectra are drawn using the spectrum recorded after applying the most aggressive thermal load {TF} as a basic line. The curves are represented in Figures 1.26 and 1.27 for type M and B polymers, respectively.

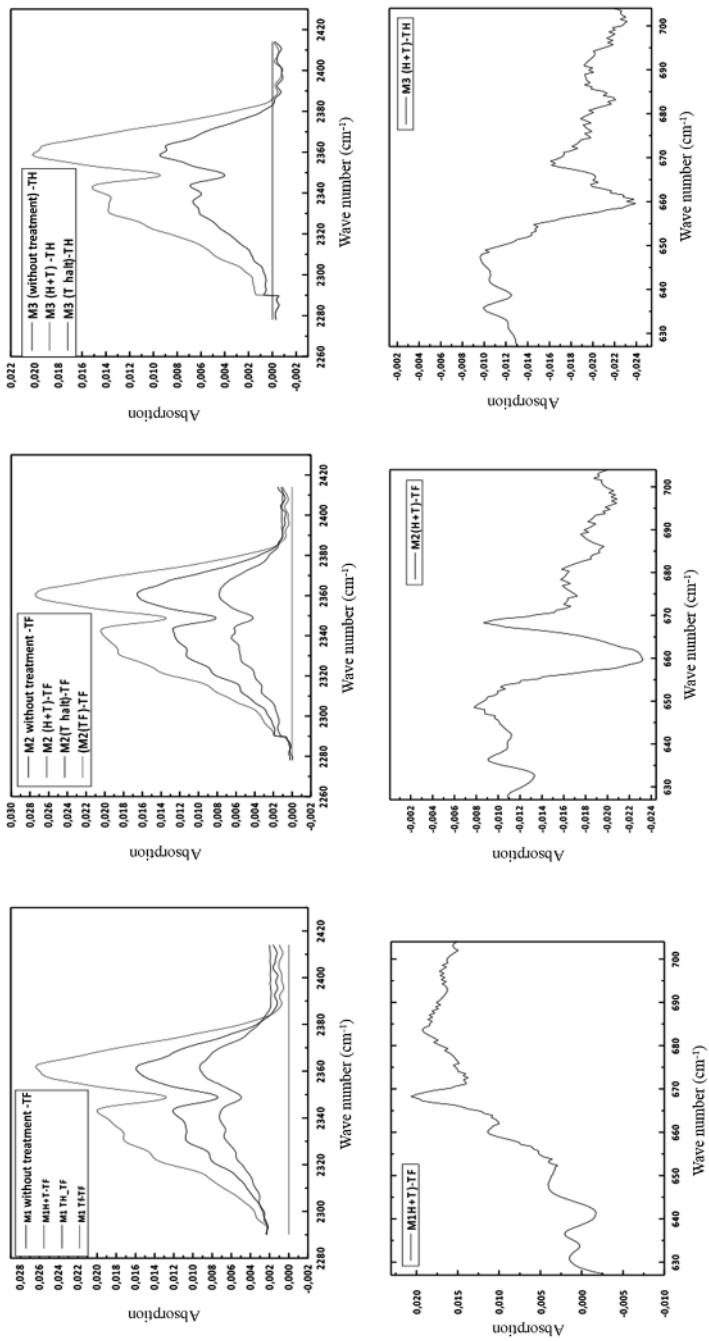

Figure 1.26. *ATR difference spectra for M-type polymers. For a color version of this figure, see www.iste.co.uk/dahoo/metrology1.zip*

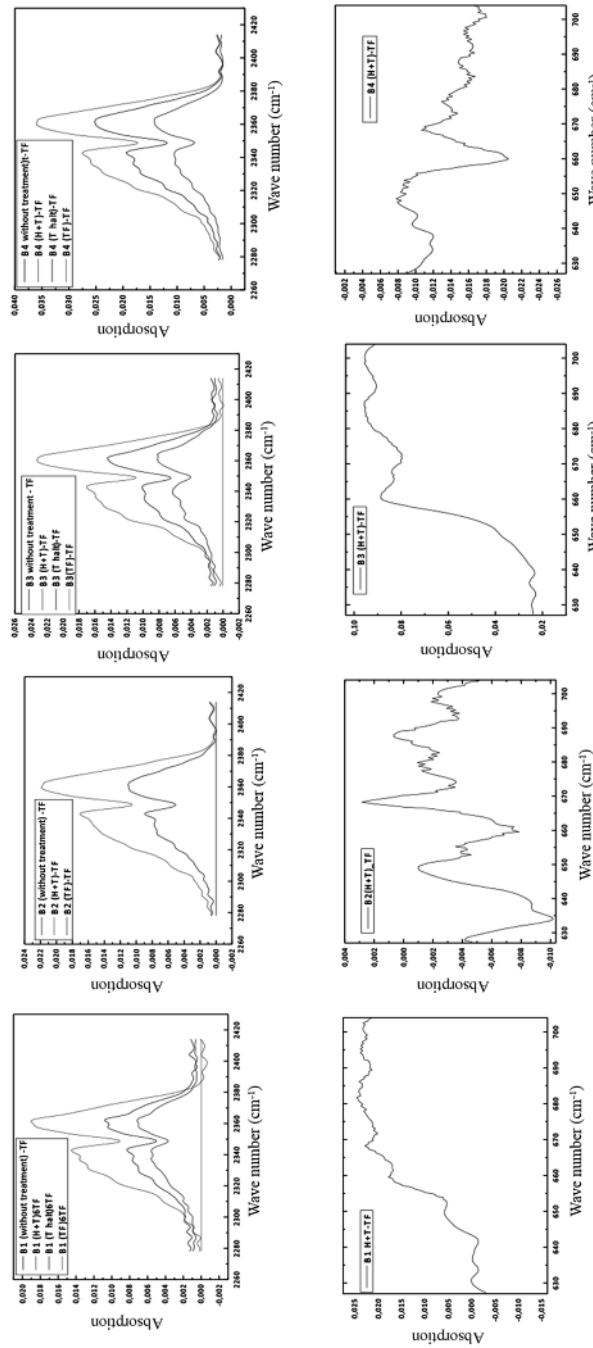

Figure 1.27. *ATR difference spectra for B-type polymers. For a color version of this figure, see www.iste.co.uk/dahoo/metrology1.zip*

The difference spectra clearly show the absorptions of CO_2 in the region of absorption in the band associated with the antisymmetric stretching approximately 2,350 cm^{-1} characterized by a branch P (low frequency) and a branch R (high frequency). The gap between the maximum of each branch is about 22 cm^{-1}. This gap is given by the formula $\Delta\nu = 2,358\sqrt{TB}$ [HER 45], where $\Delta\nu$ is expressed in cm^{-1}, B is the rotational constant of CO_2 and T is the absolute temperature. Considering a value of 0.39 cm^{-1} for B and 293 K for T, a gap of 25 cm^{-1} is calculated, which is comparable to the value measured on the spectra. In the region of atmospheric absorption of the bending mode band ν_2, the peak at 668 cm^{-1} can be observed, particularly on M-type polymers. This value can be compared with that of 667 cm^{-1}, which corresponds to the absorption in gaseous phase of this vibration that is doubly degenerate. Certain spectra feature a doublet at 650 cm^{-1}, 655 cm^{-1}, which might be associated with a degeneracy removal.

CO_2 could be simultaneously considered a Lewis acid (positive charge on the central carbon, electron acceptor) and a Lewis base (negative charge on the terminal oxygen atoms, electron donors). According to the works conducted on CO_2 in polymers [NAL 05, NAL 06, CUL 13], degeneracy removal is due to an interaction of the type Lewis acid–base between CO_2 and the groups in the polymer (ester, ether, aromatic ring, carbonyl group, etc.). Degeneracy removal is due to interactions with the carbonyl group, aromatic rings or sites with basic properties.

1.4. Conclusion

This chapter presents various deposition techniques that are used for material nano-structuring, as well as the equipment developed for sample characterization and analysis. In situ during the elaboration phase, these techniques are used to control the fabrication of materials on the nanometer scale. Some of these techniques can be used to manipulate matter at the scale of atoms. A detailed study using ATR spectroscopy, through which a material is probed by the tunnel effect over a nanometer-scale thickness, is presented. The material being pressed firmly into contact on a high-index crystal, the beam returning after total reflection is used to obtain an IR beam containing information on the spectral signature of the constituents trapped in the polymer. Absorption of CO_2 is revealed in the polymers used as encapsulation material.

1.5. Appendix: light ray propagation

In light diffraction problems, the amplitude of a wave $E_z(x,y)$ on a surface located in a plane z is determined from the amplitude $E_0(x,y)$ of a wave in the plane z = 0.

In Chapter 3 of [DAH 16], equation 3.6 gives the expression of an electromagnetic wave moving along Oz, in the form u (z-vt) = acos (k(z-ct)), where v is the wave propagation speed in a medium of index n, a its amplitude and k = 2 πn/λ. In a vacuum, n = 1 and in a three-dimensional space, the monochromatic plane wave of angular frequency ω = kc and of wave vector **k** = (kx, ky, kz) can be expressed in complex notation, in the form $\mathbf{E} = \mathbf{E_0} \exp i(2\pi/\lambda\ (\alpha x+\beta y+\gamma z) - \omega t)$, where the components of the wave vector are in the form $k_x = 2\pi\alpha/\lambda$, $k_y = 2\pi\beta/\lambda$ and $k_z = 2\pi\gamma/\lambda$, with α, β and γ being the direction cosines of the wave vector **k** and λ the wavelength. This expression can be obtained by solving the Helmholtz equation (equation 3.7, [DAH 16]):

$$\Delta\vec{\mathrm{E}} + \frac{\omega^2}{c^2}\vec{\mathrm{E}} = \vec{0} \qquad [1.1]$$

where $\Delta\vec{\mathrm{E}} = \vec{\nabla}^2\vec{\mathrm{E}}$, using the Green function $G_k(\vec{r},\vec{r}_0)$ of the Helmholtz equation, which verifies that:

$$(\nabla^2 + \mathrm{k}^2)G_k(\vec{r},\vec{r}_0) = \delta(\vec{r} - \vec{r}_0) \qquad [1.2]$$

given that: $G_k(\vec{r},\vec{r}_0) = -\frac{exp(ik|\vec{r}-\vec{r}_0|)}{4\pi|\vec{r}-\vec{r}_0|}$, and the unit vector $\vec{e}_r = \frac{(\vec{r}-\vec{r}_0)}{|\vec{r}-\vec{r}_0|}$. The solution is straightforward, and for the k mode of the electric field from a source placed in $\vec{r}_0$, we can write: $\vec{E}_k(\vec{r},\vec{r}_0) = -\frac{exp(ik|\vec{r}-\vec{r}_0|)}{4\pi|\vec{r}-\vec{r}_0|}\vec{e}_r$.

The propagation of a wave through objects (transparent apertures or opaque objects) can be determined using the Green–Ostrogradsky theorem and the Green function $G_k(\vec{r},\vec{r}_0)$ of the Helmholtz equation.

From the relation:

$$\vec{\nabla}\left(u\vec{\nabla}\mathrm{v} - \mathrm{v}\vec{\nabla}\mathrm{u}\right) = u\vec{\nabla}^2 v - v\vec{\nabla}^2 u = u\Delta v - v\Delta u \qquad [1.3]$$

where u and v are solutions of the Helmholtz equation, and from the Green–Ostrogradsky theorem, which transforms a volume integral into a surface integral:

$$\int (u\Delta v - v\Delta u)d\tau = \int \left(u\vec{\nabla}^2 v - v\nabla^2 u\right)d\tau = \oint \left(u\vec{\nabla}\mathrm{v} - \mathrm{v}\vec{\nabla}\mathrm{u}\right)d\vec{s} \qquad [1.4]$$

It can be written that:

$$\int \left(\vec{\mathrm{E}}(\vec{r})\Delta G_k(\vec{r},\vec{r}_0) - G_k(\vec{r},\vec{r}_0)\Delta\vec{\mathrm{E}}(\vec{r})\right)d\tau = \int \vec{\mathrm{E}}(\vec{r})\delta(\vec{r}-\vec{r}_0)d\tau$$

$$-\int \vec{\mathrm{E}}(\vec{r})\mathrm{k}^2 G_k(\vec{r},\vec{r}_0)d\tau + \int G_k(\vec{r},\vec{r}_0)\mathrm{k}^2\vec{\mathrm{E}}(\vec{r})d\tau = \vec{\mathrm{E}}(\vec{r}_0) \qquad [1.5]$$

Hence

$$\vec{\mathrm{E}}(\vec{r}_0) = \oint \left(\vec{\mathrm{E}}(\vec{r})\vec{\nabla}G_k(\vec{r},\vec{r}_0) - G_k(\vec{r},\vec{r}_0)\vec{\nabla}\vec{\mathrm{E}}(\vec{r})\right)d\vec{s} =$$
$$\oint\left(\vec{\mathrm{E}}(\vec{r})\left\{\vec{\nabla}G_k(\vec{r},\vec{r}_0)d\vec{s} - ikG_k(\vec{r},\vec{r}_0)ds\right\}\right) \qquad [1.6]$$

where the surface integral bounds the point located at $\vec{r}_0$ and $\vec{r}$ is the position vector of the surface element $d\vec{s}$ (Figure 1.28), such that $\vec{\nabla}\vec{\mathrm{E}}(\vec{r}).d\vec{s} = ik\vec{\mathrm{E}}(\vec{r})ds$, for a wave that propagates inwards in the volume bounded by the integral surface element ds. For a wave propagating outwards of the surface, $\vec{\mathrm{E}}(\vec{r}).d\vec{s} = -ik\vec{\mathrm{E}}(\vec{r})ds$.

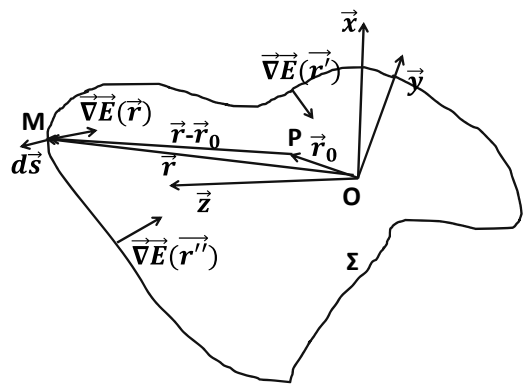

Figure 1.28. *Kirchhoff integral on a surface Σ passing through a point M enclosing the point P. For a color version of this figure, see www.iste.co.uk/dahoo/metrology1.zip*

Given that $G_k(\vec{r},\vec{r}_0) = -\frac{exp(ik|\vec{r}-\vec{r}_0|)}{4\pi|\vec{r}-\vec{r}_0|}$, it can be written that:

$$\vec{\nabla}G_k(\vec{r},\vec{r}_0) = ikG(\vec{r},\vec{r}_0)\vec{e}_r + \frac{exp(ik|\vec{r}-\vec{r}_0|)}{4\pi|\vec{r}-\vec{r}_0|^2}\vec{e}_r = \left(\frac{ik}{|\vec{r}-\vec{r}_0|} - \frac{1}{|\vec{r}-\vec{r}_0|^2}\right)(\vec{r} - \vec{r}_0)G_k(\vec{r},\vec{r}_0) \quad [1.7]$$

At a great distance compared to the wavelength such that $k|\vec{r}-\vec{r}_0| \gg 1$, the following solution is obtained:

$$\vec{\mathrm{E}}(\vec{r}_0) = \oint\left(\vec{\mathrm{E}}(\vec{r})\left\{\frac{ik}{|\vec{r}-\vec{r}_0|}(\vec{r}-\vec{r}_0)G_k(\vec{r},\vec{r}_0)d\vec{s} - ikG_k(\vec{r},\vec{r}_0)ds\right\}\right) \quad [1.8]$$

such that:

$$\vec{\mathrm{E}}(\vec{r}_0) = -\frac{ik}{4\pi}\oint\vec{\mathrm{E}}(\vec{r})\frac{exp(ik|\vec{r}-\vec{r}_0|)}{|\vec{r}-\vec{r}_0|^2}\left((\vec{r}-\vec{r}_0)d\vec{s} - |\vec{r}-\vec{r}_0|ds\right) \quad [1.9]$$

This solution is the mathematical formulation of the Huygens–Fresnel principle or the Huygens–Fresnel equation obtained by the Kirchhoff integral. Hence, it is the Fresnel–Kirchhoff diffraction formula.

When a monochromatic plane wave propagating parallel to Oz encounters a screen (E_0) with an opening (Figure 1.29), a diffraction pattern is formed in the observation plane. To simplify, the plane of the opening is supposed to be perpendicular to the propagation of the plane wave and that the amplitude and the gradient of the electric field of the wave are constant on the surface of the opening located in the vicinity of M (Figure 1.28) and zero elsewhere. The amplitude on the other side of the aperture at a point P located at $\vec{r}_0$ is given by the Fresnel–Kirchhoff diffraction formula. If the opening is in the Oxy plane (Figure 1.29), and the dimensions are small compared to the position of the point P located at $\vec{r}_0$, the amplitude of the field at P writes as:

$$\vec{\mathrm{E}}(\vec{r}_0) = -\frac{ik\vec{\mathrm{E}}(\vec{r})}{4\pi R}(cos\theta + 1)\oint exp(ik|\vec{r}-\vec{r}_0|)dxdy \quad [1.10]$$

where R is the distance between the center of the opening and the point P (as a first approximation, it is the same distance for all the points of the opening), and θ is the angle between the axis Oz and the vector $\overrightarrow{MP} = \vec{r}_0 - \vec{r}$. The origin of the coordinates system is the plane containing the diffracting opening.

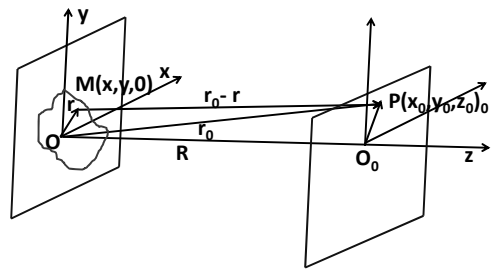

Figure 1.29. *Schematic of the diffraction by an aperture scanned by M in a plane at point P. For a color version of this figure, see www.iste.co.uk/dahoo/metrology1.zip*

The modulus of vector $\vec{r}_0 - \vec{r}$ is given by: $|\vec{r}_0 - \vec{r}| = \sqrt{r_0^2 - 2\vec{r}_0.\vec{r} + r^2}$.

Under the far-field Fraunhofer diffraction conditions, with an origin O in the plane of the aperture (Figure 1.29), where R is the distance between the observation plane and the diffracting plane, we can write that:

$$exp(ik|\vec{r} - \vec{r}_0|) = exp\left(ik\sqrt{r_0^2 - 2\vec{r}_0.\vec{r} + r^2}\right)$$
$$= e^{ikR}exp\big(-ik(\alpha x + \beta y)\big) \qquad [1.11]$$

where: $\alpha = \frac{x_0}{R}$ and $\beta = \frac{y_0}{R}$.

In the case of the Gaussian approximation, with paraxial light rays, the field at P is expressed as:

$$\vec{\mathrm{E}}(\vec{r}_0) = \mathrm{A}\oint\!\!\oint exp\big(-ik(\alpha x + \beta y)\big)dxdy \qquad [1.12]$$

We can thus calculate the Fraunhofer diffraction at a far distance by this formula. In the case of a circular aperture, it can be written as:

$$\vec{\mathrm{E}}(\vec{r}_0) = \mathrm{A}\iint exp\big(-ik(\alpha\rho cos\varphi)\big)\rho d\rho d\varphi$$

$$= 2\pi A\int_0^a J_0(k\alpha\rho)\rho d\rho = 2\pi A a^2\frac{J_1(k\alpha\rho)}{k\alpha\rho} \qquad [1.13]$$

where $J_0(x)$ and $J_1(x)$ are the Bessel functions of zeroth and first orders, respectively.

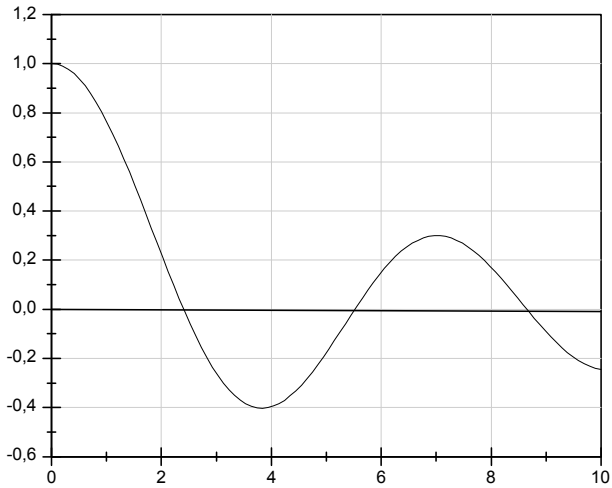

Figure 1.30. *Diffraction amplitude distribution by a circular aperture. For a color version of this figure, see www.iste.co.uk/dahoo/metrology1.zip*

Fresnel diffraction is localized in an observation plane closer to the aperture than a distance of $\lambda/2\pi$. In this case, the terms of order 2 in x and y must be considered and it is wise to use a coordinate system so as to get rid of the terms of order 1 in x and y. The aperture is placed in the Oxy plane with the Oz axis, which is perpendicular to the plane passing through the observation point r_0. In this coordinate system, $\alpha = \beta = \vec{r}.\vec{r}_0$=0. Under such conditions, the following expression is calculated:

$$exp(ik|\vec{r} - \vec{r}_0|) = exp\left(ik\sqrt{r_0^2 - 2\vec{r}_0.\vec{r} + r^2}\right) = e^{ikR}exp\left(\frac{ik(x^2+y^2)}{2R}\right) \quad [1.14]$$

In the case of the Gaussian approximation, with paraxial light rays, the field at P is expressed as:

$$\vec{E}(\vec{r}_0) = A \int exp\left(\frac{ikx^2}{2R}\right) dx \int exp\left(\frac{iky^2}{2R}\right) dy \quad [1.15]$$

From which it is possible to calculate the Fresnel diffraction pattern.